Using Virtual Testing for

Characterization of Composite Materials

by

Joseph Harrington

A Thesis Presented in Partial Fulfillment
of the Requirements for the Degree
Master of Science

Approved January 2015 by the
Graduate Supervisory Committee:

Subramaniam Rajan, Chair
Narayanan Neithalath
Barzin Mobasher

ARIZONA STATE UNIVERSITY

May 2015

ABSTRACT

Composite materials are finally providing uses hitherto reserved for metals in structural systems applications – airframes and engine containment systems, wraps for repair and rehabilitation, and ballistic/blast mitigation systems. They have high strength-to-weight ratios, are durable and resistant to environmental effects, have high impact strength, and can be manufactured in a variety of shapes. Generalized constitutive models are being developed to accurately model composite systems so they can be used in implicit and explicit finite element analysis. These models require extensive characterization of the composite material as input. The particular constitutive model of interest for this research is a three-dimensional orthotropic elasto-plastic composite material model that requires a total of 12 experimental stress-strain curves, yield stresses, and Young's Modulus and Poisson's ratio in the material directions as input. Sometimes it is not possible to carry out reliable experimental tests needed to characterize the composite material. One solution is using virtual testing to fill the gaps in available experimental data. A Virtual Testing Software System (VTSS) has been developed to address the need for a less restrictive method to characterize a three-dimensional orthotropic composite material. The system takes in the material properties of the constituents and completes all 12 of the necessary characterization tests using finite element (FE) models. Verification and validation test cases demonstrate the capabilities of the VTSS.

ACKNOWLEDGEMENTS

Thank you to Dr. Rajan for all of the opportunities you have provided me. I cannot thank you enough for your guidance and mentorship. Thank you to Dr. Neithalath and Dr. Mobasher for serving as my committee members. I appreciate all of the knowledge I have gained from you both in the field of composites. Also, I am grateful for the support of the Federal Aviation Administration through Grant #12-G-001 entitled "Composite Material Model Impact Analysis", William Emmerling, technical mentor. Finally, thank you to the rest of the MAT213 team members including Robert K. Goldberg, Kelly S. Carney, Paul Du Bois, Canio Hoffarth, and Gunther Blankenhorn.

TABLE OF CONTENTS

Page

CHAPTER Page

CHAPTER Page

LIST OF FIGURES

Figure Page

Figure Page

Figure Page

Figure Page

LIST OF TABLES

Table Page

Table Page

NOMENCLATURE

F_i = Tsai-Wu Yield Function Coefficient

σ_{45}^{i-j} = Stress 45° from the i-j Material Coordinate System Plane

J_2 = Second Invariant of the Deviatoric Stress Tensor

σ_{kk} = Trace of the Stress Tensor

α = State Variable Controlling the Influence of Hydrostatic Stress Effects

1 INTRODUCTION

1.1 Motivation for Research and Overview

Composite materials are finally providing uses hitherto reserved for metals in structural systems applications – airframes and engine containment systems, wraps for repair and rehabilitation, and ballistic/blast mitigation systems. They have high strength-to-weight ratios, are durable and resistant to environmental effects, have high impact strength, and can be manufactured in a variety of shapes. Generalized constitutive models are being developed to accurately model composite systems so they can be used in implicit and explicit finite element (FE) analysis. These models require extensive characterization of the composite material as input. The particular constitutive model of interest for this research is the three-dimensional orthotropic elasto-plastic composite material model being implemented in LS-DYNA as MAT213 (R. K. Goldberg et al., 2014; Hoffarth et al., 2014). The input for this model includes a total of 12 experimental stress-strain curves, yield stresses, and Young's Modulus and Poisson's ratio in the material directions. Sometimes it is impractical to carry out reliable experimental tests needed to characterize the composite material. One solution is using virtual testing to fill the gaps in available experimental data.

1.2 Literature Review

The major focus of this research is using virtual tests for characterization of composite materials. The intent of most current virtual testing suites is for use as a design tool, modeling the damage and failure mechanisms of composite materials through multiscale analysis. The multiscale analysis ranges from micromechanical analysis of the

constituent properties to modeling entire structural components. Depending on the method, the process of homogenization or localization between the different length and time scales can be complex and add significant computation time.

There are numerous composite homogenization and localization techniques. The earliest, most simplistic method being the rule of mixtures (Voigt, 1890). As composites gained popularity, more refined methods emerged, including Eshelby's formula (Eshelby, 1957) and Aboudi's generalized method of cells (Aboudi, 2004). However, these methods are more restrictive than the fully numerical methods, such as the finite element method.

The particular component of multiscale analysis pertinent to this research is homogenizing constituent level analysis to obtain structural level properties. One computational approach is the Hill-Mandel condition, which requires the variation of work be equivalent between the macroscopic volume average of the RVE and locally on the macro-scale (Hill, 1963; Suquet, 1985). Furthermore, for an RVE with kinematic boundary conditions, the macroscopic stress tensor is equivalent to the volume average of the microscopic stress tensor (Coenen, Kouznetsova, & Geers, 2012). This formulation and the results from Melro et al. (Melro, Camanho, & Pinho, 2012) indicating that a 'volumetric homogenization' produces accurate results for the response of composite materials is the basis for Okereke and Akpoyomare (Okereke & Akpoyomare, 2013) implementing this homogenization technique within their virtual testing framework.

One example of integrating homogenization and localization techniques into a multiscale design and analysis suite is ImMAC developed by Bednarcyk et al., which

supports nonlinear micromechanics integrated within higher scale FE analysis (Bednarcyk, NASA Glenn Research Center, & United States, 2012). Using the generalized method of cells at the micro scale to model the nonlinear deformation and damage of the composite, the need to implement a complex model to handle this response at higher levels is avoided. However, this leads to using five levels of scale for the simulations, significantly increasing the computation time.

A Virtual Testing Software System (VTSS) has been developed to address the need for a less restrictive method to characterize a three-dimensional orthotropic composite material. The system takes in the material properties of the constituents and completes all 12 of the necessary characterization tests using FE models. One way in which the method is less restrictive is the assumption of a perfect fiber-matrix interface. This common assumption allows for increased computational efficiency. For example, Duschlbauer et al. present computation simulations of reinforced composites using unit cell based periodic microfield and extended Mori-Tanaka mean field approaches assuming a perfect fiber-matrix interface (Duschlbauer, BÖhm, & Pettermann, 2006). An extended Mori-Tanaka approach is necessary because previous attempts of modeling non-spherical reinforcements (e.g., fibers) indicated that the method is only applicable for aligned reinforcement. However, the new extended method developed provides good agreement with the periodic unit cell approach for the effective composite properties presented. While this indicates that the computationally inexpensive extended Mori-Tanaka approach is applicable for this particular composite, it is only one test case and the authors suggest it is only applicable for most purposes. Another limitation comes

from the short fibers with planar random orientation formulation, both contributing to increased computation time.

The approximation of perfect fiber-matrix interface removes the need for further testing to characterize the cohesive elements used by a number of the virtual testing suites to model this interface. Davies and Ankersen investigate virtual testing of composite structures using cohesive interface elements between components (Davies & Ankersen, 2008). This allows for modeling of delamination or debonding, but requires additional testing to determine an accurate representation of these cohesive elements. A local/global analysis is implemented where the course mesh of the entire structure has areas of interest meshed much finer. This requires applying tractions/displacements at the boundaries. While this lends itself to computational efficiency, especially with parallel processing, because the analysis of each region can be separated, the authors acknowledge there is no proof to the validity of this approach.

Llorca et al. present an integrated design strategy, which includes a multiscale simulation strategy where the analysis ranges from the micromechanics of an RVE to the computational mechanics of structural components (LLorca et al., 2011; Llorca, González, Molina-Aldareguía, & Lópes, 2013). Cohesive elements are used to model the fiber-matrix interaction within the RVE, allowing for a more accurate representation of damage and failure mechanisms in the composite. However, this adds another level of complexity with difficult testing needed to characterize the constituent materials.

Another framework that includes cohesive elements is presented by Yang et al., which implements multi-scale analysis within an augmented-finite element method (A-

FEM) (Yang, Cox, Fang, & Zhou, 2010). The advantage of A-FEM over X-FEM is that the elements utilize only standard FE shape functions as opposed to the partition-of-unity used in X-FEM, resulting in seamless integration with FE programs. The key distinction from the previous cohesive elements and those used by Yang et al. is the ability to split into separate elements. This allows for a more accurate modeling of composite cracking, which is a common observed damage mode. However, this adds significant computation time to the simulation along with the aforementioned difficult constituent characterization testing.

Another simplification within the VTSS approach is the uniform fiber placement. While typical manufacturing procedures result in randomly placed fibers, the response in virtual testing can be insensitive to fiber randomness. This was the case for the predicted peak strength comparison reported by Yang et al. using the A-FEM (Yang et al., 2010).

The idea of balancing modeling approximations and computational efficiency is present in all virtual testing suites. One example is seen in FEAMAC, developed at NASA Glenn Research Center by Bednarcyk et al., which justifies modeling failure through a reduction in stiffness as opposed to complete separation of the fiber and matrix interface due to the fiber dominated nature of the failure mechanism observed in a longitudinal tensile test (Bednarcyk et al., 2012). In this way, the addition of unnecessary complexity to the model to enhance already representative analysis is avoided. This general idea is the basis for excluding multiscale analysis from the VTSS. Replicating experimental testing with explicit modeling of the constituents is expected to be representative of the material behavior for the required composite material

characterization. This is investigated through test cases comparing results from the VTSS against available experimental and computed data.

One test case replicates the results presented by Okereke and Akpoyomare, which includes experimental data to validate their virtual framework for characterizing composites (Okereke & Akpoyomare, 2013). The framework presented by Okereke and Akpoyomare is limited to the elastic response of continuous unidirectional composites. Also, the Monte Carlo style geometric model generation algorithm and the periodic boundary conditions significantly increase the required computational time. Further discussion on this, and other, test cases is contained in the following section.

1.3 Thesis Objectives

The focus of this research is to develop the VTSS, verify, and validate the method using different test cases. The purpose of the first test case is to determine if the approximations have a significant impact on the results of the elastic engineering constants. As previously mentioned, most of the current virtual testing suites are used as design tools, therefore, only a limited number are used to characterize engineering constants (Duschlbauer et al., 2006; Okereke & Akpoyomare, 2013). The boron-aluminum composite test results from the virtual testing framework developed by Okereke and Akpoyomare were selected for reproduction by the VTSS because both formulations use continuous unidirectional fiber composite geometry. The virtual framework has limitations including overly restrictive boundary conditions, isotropic constituent materials, and that it is limited to an elastic analysis.

It is necessary to complete a second test case to demonstrate capabilities of the VTSS to incorporate plasticity with anisotropic constituent materials to produce the other portion of the MAT213 input – stress-strain curves. The T800S/3900-2B [P2352W-19] BMS8-276 Rev-H-Unitape manufactured by Toray and used by Boeing in its 787 Dreamliner airplane is used for this test case. Toray describes T800S as an intermediate modulus, high tensile strength graphite fiber. The epoxy resin system is a toughened epoxy combined with small elastomeric particles to form a compliant interface or interleaf between fiber plies to resist impact damage and delamination. After completing the necessary tests using the VTSS, the results are compared against MAC/GMC along with the limited baseline experimental data available from tests completed at Wichita State University (Raju & Acosta, 2010). In addition, this test case also includes an investigation of modeling plasticity in the matrix using a von Mises plasticity model versus a polymer plasticity model, which accounts for hydrostatic stress effects.

2 COMPOSITES

2.1 Characterization

The testing required to characterize a three-dimensional orthotropic material behavior, with specific consideration for MAT213 input, is discussed in this section. MAT213 theoretical details are detailed in a companion paper (R. K. Goldberg et al., 2014). The generalized Hooke's Law for 3D orthotropic materials is shown in Eqn. (2.1).

$$\begin{bmatrix} \sigma_1 \\ \sigma_2 \\ \sigma_3 \\ \tau_4 \\ \tau_5 \\ \tau_6 \end{bmatrix} = \begin{bmatrix} \frac{1}{E_{11}} & -\frac{\nu_{21}}{E_{22}} & -\frac{\nu_{31}}{E_{33}} & 0 & 0 & 0 \\ & \frac{1}{E_{22}} & -\frac{\nu_{32}}{E_{33}} & 0 & 0 & 0 \\ & & \frac{1}{E_{33}} & 0 & 0 & 0 \\ & & & \frac{1}{G_{12}} & 0 & 0 \\ & Sym & & & \frac{1}{G_{23}} & 0 \\ & & & & & \frac{1}{G_{31}} \end{bmatrix}^{-1} \begin{bmatrix} \varepsilon_1 \\ \varepsilon_2 \\ \varepsilon_3 \\ \gamma_4 \\ \gamma_5 \\ \gamma_6 \end{bmatrix} \tag{2.1}$$

The engineering constants contained in Eqn. (2.1) are part of the input for MAT213. Tension, compression, and shear tests in all material directions and planes are necessary to determine these parameters. MAT213 also requires additional input in the form of stress-strain curves to determine the yield function coefficients for the Tsai-Wu yield surface defined in Eqn. (2.2).

$$\begin{aligned} \mathbf{f}(\boldsymbol{\sigma}) = a + F_1\sigma_{xx} + F_2\sigma_{yy} + F_3\sigma_{zz} + F_{11}\sigma_{xx}^2 + 2F_{12}\sigma_{xx}\sigma_{yy} + 2F_{13}\sigma_{xx}\sigma_{zz} \\ + F_{22}\sigma_{yy}^2 + 2F_{23}\sigma_{yy}\sigma_{zz} + F_{33}\sigma_{zz}^2 + F_{44}\sigma_{xy}^2 + F_{55}\sigma_{yz}^2 + F_{66}\sigma_{zx}^2 \end{aligned} \tag{2.2}$$

where

$$\begin{aligned} F_1 &= \frac{1}{\sigma_{11}^T} - \frac{1}{\sigma_{11}^C} \quad F_{11} = \frac{1}{\sigma_{11}^T \sigma_{11}^C} \quad F_{44} = \frac{1}{\sigma_{12}^2} \\ F_2 &= \frac{1}{\sigma_{22}^T} - \frac{1}{\sigma_{22}^C} \quad F_{22} = \frac{1}{\sigma_{22}^T \sigma_{22}^C} \quad F_{55} = \frac{1}{\sigma_{23}^2} \\ F_3 &= \frac{1}{\sigma_{33}^T} - \frac{1}{\sigma_{33}^C} \quad F_{33} = \frac{1}{\sigma_{33}^T \sigma_{33}^C} \quad F_{66} = \frac{1}{\sigma_{31}^2} \end{aligned} \tag{2.3}$$

and the off-diagonal yield function coefficients are defined as

$$F_{ij} = \frac{2}{\left(\sigma_{45}^{i-j}\right)^2} - \frac{F_i + F_j}{\sigma_{45}^{i-j}} - \frac{1}{2}(F_{ii} + F_{jj} + F_{kk}) \quad i, j = 1,2,3, k = i + 3 \tag{2.4}$$

The full stress-strain curve for each test corresponding to the stress components of the yield function coefficients shown in Eqns. (2.3) and (2.4) are needed to describe the hardening properties of the composite as it varies with effective plastic strain. The 12 tests and the associated MAT213 input required to characterize an orthotropic composite material is summarized in Appendix A.

While many of these tests are prescribed by ASTM standards (D30 Committee, 2007, 2008, 2011, 2013, 2014), even these tests can still be difficult to complete. An example of this is the through-thickness tension test. Because most composite applications are driven by the strength-to-weight savings of the material, it is not common to manufacture composites thick enough to allow for tension testing in the through-thickness direction using a dogbone specimen. Therefore, many approaches (Adams, 2009; Karkkainen, Moy, & Tzeng, 2009; Vali-shariatpanahi, 2009) suggest slight modifications to the ASTM (D30 Committee, 2007) including further reduction of

the cross-sectional area in the gage length, beveling specimen ends to increase the contact surface area for the epoxy, and using notches in the grips and specimen, among others. However, again due to the size of the specimen, it can be difficult to accomplish the associated manufacturing procedures without introducing delamination or other flaws into the material. This example illustrates the difficulty of experimental testing and how virtual testing is often a necessary supplemental tool for material characterization.

2.2 Plasticity Model

An important component of the virtual testing is modeling plasticity. One of the most common plasticity models, von Mises plasticity, is initially used to describe plasticity in the matrix for the second test case. For von Mises plasticity, plastic yielding begins when the deviatoric elastic strain-energy reaches a critical value (Neto, Periæ, & Owen, 2009, p. 162). Because of this formulation, the von Mises yield function is solely dependent on the deviatoric component of the stress. It will never predict yielding for a purely hydrostatic stress state.

Although appropriate to describe plasticity in many metals, not all materials follow von Mises plasticity. Some materials are hydrostatic stress state dependent and inclusion of these effects in the plasticity model is necessary to accurately model the material response. Therefore, a polymer plasticity model that accounts for these effects is investigated (R. Goldberg, Roberts, & Gilat, 2005). The Drucker-Prager yield criterion, a pressure-dependent model, is the basis for the inelastic potential function shown in Eqn. (2.5).

$$f = \sqrt{J_2} + \alpha\sigma_{kk} \tag{2.5}$$

where J_2 is the second invariant of the deviatoric stress tensor, σ_{kk} is the trace of the stress tensor, and α is a state variable controlling the influence of hydrostatic stress effects. The theoretical details of this polymer plasticity model are not presented here. Rather, this introduction illustrates the incorporation of hydrostatic stress effects, distinguishing it from von Mises plasticity. The second test case includes a comparison of the results from both plasticity models described in this section against experimental data to determine which is more accurate in modeling plasticity in the matrix of the T800S/3900 composite material.

3 VIRTUAL TESTING METHODOLOGY & VTSS SYSTEM

Testing methodology for a two-phase unidirectional composite material is discussed in this section. The basic architecture of a continuous unidirectional fiber composite is shown in Figure 3.1.

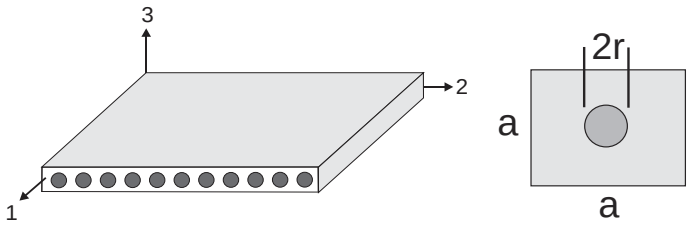

(a) (b)

Figure 3.1 (a) Single Ply of a Continuous Unidirectional Laminated Composite and (b) Unit Cell

A typical cross-section used in a test is shown in Figure 3.2.

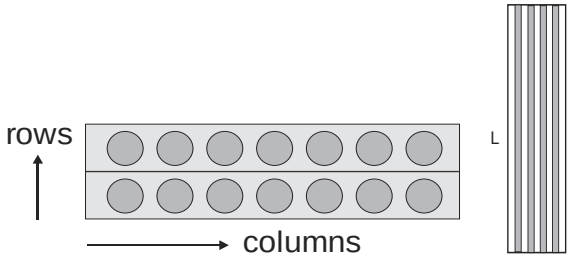

(a) (b)

Figure 3.2 (a) Typical Stack of Unit Cells in a Test (Shown With 2 Rows and 7 Columns) and (b) Plan View Showing Length of the Specimen

The parameters shown are input into the VTSS to characterize the geometry of the test specimen.

3.1 Finite Element Analysis

A quasi-static finite element analysis is carried out. The elements used to mesh the composite include wedge elements, used in the fibers, and hexahedral elements, used in the fibers and matrix.

3.2 Test Procedures

The boundary condition details for each of the 12 tests necessary to characterize a general orthotropic material are described in this section. A displacement controlled analysis is carried out for each test. The applied displacement is determined as to produce a similar total strain as the available computed and experimental data when available. The visual depiction in Figure 3.3 is supplemented by a written description for each test. The finite element models with the boundary conditions displayed are used for the off-axis tests due to the difficulty of visually representing the test without the entire model. For the remaining tests, smaller representative models are used. Although the fibers are shown only on the front face, they are continuous. The faces with applied boundary conditions are highlighted in a light red and the applied boundary conditions themselves are a darker shade of red. The tension and compression test procedures are identical with the exception of the direction of the applied displacements.

3.2.1 Tension/Compression Test – 1-Direction

Nodes on the front face are fixed in the 1-direction. Nodes at the middle of this face are also fixed in the 2 and 3-directions. Displacements are applied to the nodes on the back face in the 1-direction.

3.2.2 Tension/Compression Test – 2-Direction

Nodes on the right face are fixed in the 2-direction. Nodes at the middle of this face are also fixed in the 1 and 3-directions. Displacements are applied to the nodes on the left face in the 2-direction.

3.2.3 Tension/Compression Test – 3-Direction

Nodes on the top face are fixed in the 3-direction. Nodes at the middle of this face are also fixed in the 1 and 2-directions. Displacements are applied to the nodes on the bottom face in the 3-direction.

3.2.4 Pure Shear Test – 1-2 Plane

Nodes on the right face are pinned. Displacements are applied to the nodes on the left face in the 1-direction.

3.2.5 Pure Shear Test – 2-3 Plane

Nodes on the top face are pinned. Displacements are applied to the nodes on the bottom face in the 2-direction.

3.2.6 Pure Shear Test – 1-3 Plane

Nodes on the top face are pinned. Displacements are applied to the nodes on the bottom face in the 1-direction.

Because of the formulation of the models, the entire test specimen is modeled for the off-axis tests, similar to a physical tension test with a clamped section on either side (referred to as displacement and pinned sections).

3.2.7 Off-Axis Test – 45°, 1-2 Plane

Nodes in the pinned section are fixed in all directions. Displacements are applied at 45° to the 1-direction in the 1-2 plane.

3.2.8 Off-Axis Test – 45°, 2-3 Plane

Nodes in the pinned section are fixed in all directions. Displacements are applied at 45° to the 2-direction in the 2-3 plane.

3.2.9 Off-Axis Test – 45°, 1-3 Plane

Nodes in the pinned section are fixed in all directions. Displacements are applied at 45° to the 1-direction in the 1-3 plane.

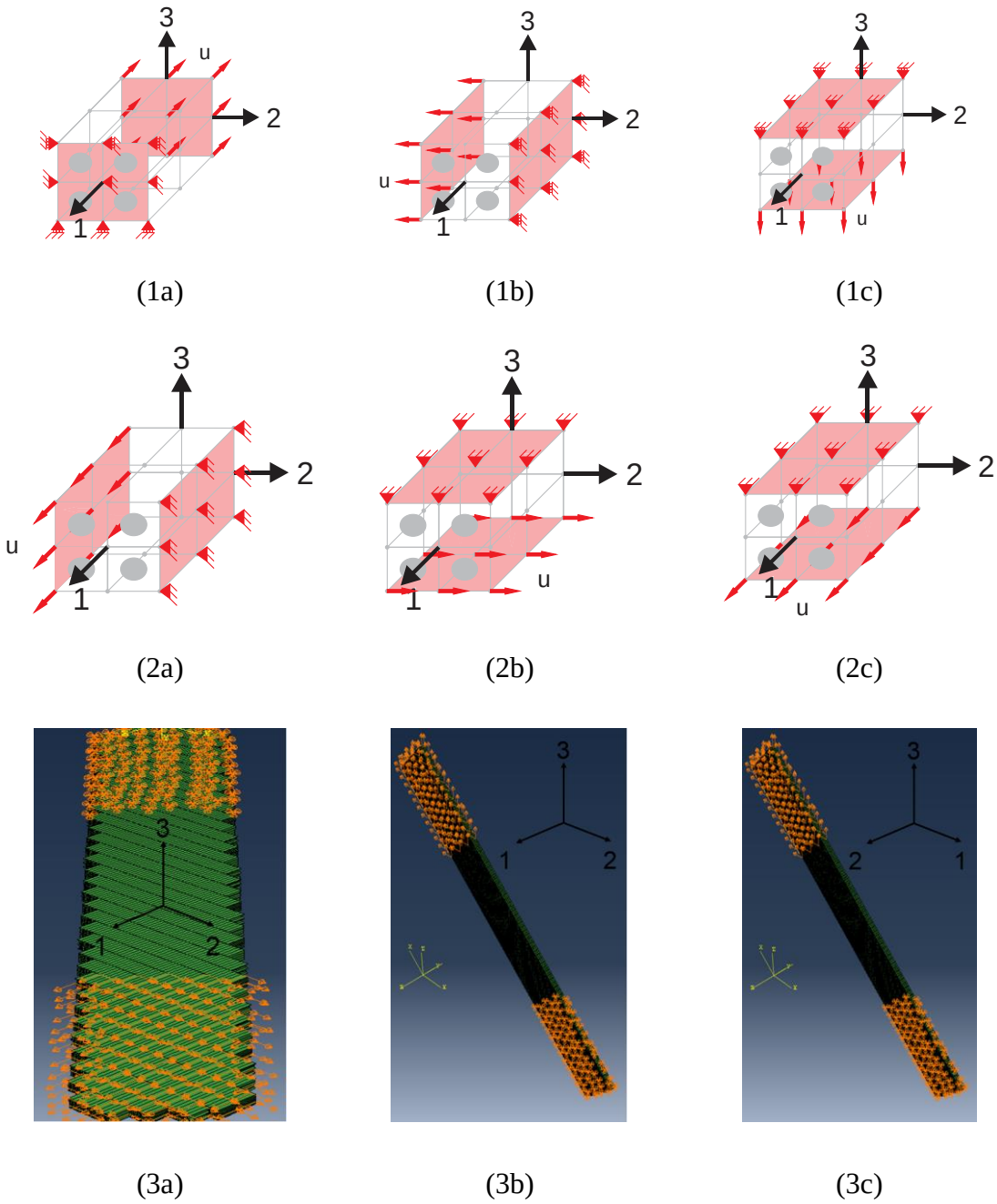

Figure 3.3 Boundary Conditions for (1) Tension/Compression Tests in the (a) 1, (b) 2, and (c) 3-directions, (2) Pure Shear Tests in the (a) 1-2, (b) 2-3, and (c) 1-3 Planes, and (3) Off-Axis Tests in the (a) 1-2, (b) 2-3, and (c) 1-3 Planes

3.3 Post-Processing

The method used to compute the homogenized response of the composite is a simple volumetric averaging of the results from the finite element analysis. One requirement of this method is that the post-processed section is volumetrically representative of the entire specimen. The post-processed region is taken as the thickness of the test specimen in the direction perpendicular to the applied loading as close to the center of the test specimen and sufficiently far away from the applied boundary conditions (similar to establishing the gage length of a specimen used for experimental testing). The stress and strain results are averaged using Eqn. (3.1) and are used to calculate the necessary homogenized material properties.

$$\bar{P}_h \equiv \frac{\sum_{j=1}^{e_t} \left(\frac{\sum_{i}^{n_{e_t}} \bar{P}_i V_i}{\sum_{i}^{n_{e_t}} V_i} \right)_j V_j}{\sum_{j=1}^{e_t} V_j} \tag{3.1}$$

where

$\bar{P}_h$ is the homogenized material property

e_t is the number of different element types

n_{e_t} is the number of elements in the jth element type

$\bar{P}_i$ is the material property for the ith element calculated from the stresses and strains averaged over the total number of integration points for the element

V_i is the volume of the ith current element

4 NUMERICAL RESULTS

The results from the VTSS test cases for a two-phase unidirectional composite material are compared against available experimental and computed data and discussed in this section.

4.1 Test Case 1: Virtual Framework for Prediction of Full-field Elastic Response of Unidirectional Composites

The available boron-aluminum composite results from the virtual framework developed by Okereke and Akpoyomare are replicated using the VTSS and reported in the subsequent sections.

4.1.1 Material Properties

The tests are completed using the assumption that the fiber and matrix are linear, elastic with engineering constants shown in Table 4.1.

Table 4.1 Material Properties used in Boron-Aluminum Tests

Engineering Constant	Fiber (Boron)	Matrix (Aluminum)
E (GPa)	379.3	68.3
ν	0.1	0.3
G (GPa)	172.4	26.3

4.1.2 Composite Geometry

Using the information provided in the report for the FEM Big framework, the parameters needed to define the VTSS specimen geometry are calculated. With a volume fraction of 47%, window size of 100 μm^2, and 27 fibers, the fiber radius is calculated as 0.744 μm and the length of each side of the unit cell is 1.925 μm. The overall test specimen included 5 rows and columns to approximate the 100 μm^2 window size.

4.1.3 Homogenized Material Properties

Completing each test as described in the Test Procedures section allows for the following comparisons between the VTSS results and those presented by Okereke and Akpoyomare, shown in Table 4.2

Table 4.2 Comparison of Predictions of the Effective Elastic Properties of Boron-Aluminum Composite

Elastic Constants (GPa)	Experiment (Kenaga)	FEM Small	FEM Big	FEM Sun (Square/ Hexagonal)	Analytical (Hashin and Rosen)	Semi-Empirical (Chamis)	VTSS
E_{11}	216.0	215.0	214.0	215.0/215.0	215.0	214.0	214.3
E_{22}	140.0	141.0	134.0	144.0/136.5	139.1	156.0	142.4
E_{33}	-	141.0	135.0	-	-	-	142.4
ν_{12}	0.290	0.195	0.196	0.19/0.19	0.195	0.200	0.196
ν_{13}	-	0.195	0.194	-	-	-	0.195
ν_{23}	-	0.255	0.302	0.29/0.34	0.310	0.310	0.247
G_{12}	52.0	51.9	52.0	57.2/54.0	53.9	62.6	54.3
G_{13}	-	52.0	52.8	-	-	-	54.3
G_{23}	-	45.0	49.4	45.9/52.5	54.6	43.6	46.1

4.2 Test Case 2: T800S/3900 Tests

The homogenized engineering stress-strain curves produced by the VTSS are compared against computed and experimental data of the T800S/3900 composite when available. The computed data is from the Micromechanics Analysis Code based on the Generalized Method of Cells (MAC/GMC) software. The experimental data is from the aforementioned tests completed by Raju and Acosta at Wichita State University (WSU). The availability of experimental data for the tests necessary to produce the input for MAT213 is summarized in Table 4.3.

Table 4.3 Availability of Experimental Data for MAT213 Input Tests

Test	Experimental Data
Tension Test (1-Direction)	Available
Tension Test (2-Direction)	Not available
Tension Test (3-Direction)	Use transverse isotropy
Compression Test (1-Direction)	Available
Compression Test (2-Direction)	Not available
Compression Test (3-Direction)	Use transverse isotropy
Pure Shear Test (1-2 Plane)	Available
Pure Shear Test (2-3 Plane)	Not available
Pure Shear Test (1-3 Plane)	Use transverse isotropy
Off-Axis Test (45°, 1-2 Plane)	Not available
Off-Axis Test (45°, 2-3 Plane)	Not available
Off-Axis Test (45°, 1-3 Plane)	Use transverse isotropy

For the tests where experimental data is available, three samples were tested by WSU. Each sample is included in the stress-strain curves comparing the results. For the tests where experimental data is not available, the stress-strain curve from the virtual finite element test is compared against the MAC/GMC results.

4.2.1 Material Properties

The orthotropic composite test cases are completed using the assumption that the fiber (transversely isotropic) is linear, elastic and the matrix (isotropic) is elasto-plastic. As identified in other virtual testing suites (LLorca et al., 2011), the characterization process of the constituent materials included gathering available properties for the fibers (Torayca, 2003) and additional testing for the matrix. Optimization of the matrix material properties was completed through correlating the results from MAC/GMC to the available WSU experimental data (R. K. Goldberg, 2013). The results for the engineering constants are shown in Table 4.4.

Table 4.4 Material Properties used in T800S/3900 Tests

Engineering Constant	Fiber (psi)	Matrix (psi)
E_1 (psi)	$4(10^7)$	$5(10^5)$
E_2, E_3 (psi)	$2.25(10^7)$	$5(10^5)$
ν_{12}, ν_{13}	0.2	0.35
ν_{23}	0.25	0.35
G_1 (psi)	$1.5(10^7)$	$1.85(10^5)$
G_2, G_3 (psi)	$1.5(10^7)$	$1.85(10^5)$

The assumed elasto-plastic behavior with strain hardening for the matrix is defined using a stress-strain curve in Figure 4.1.

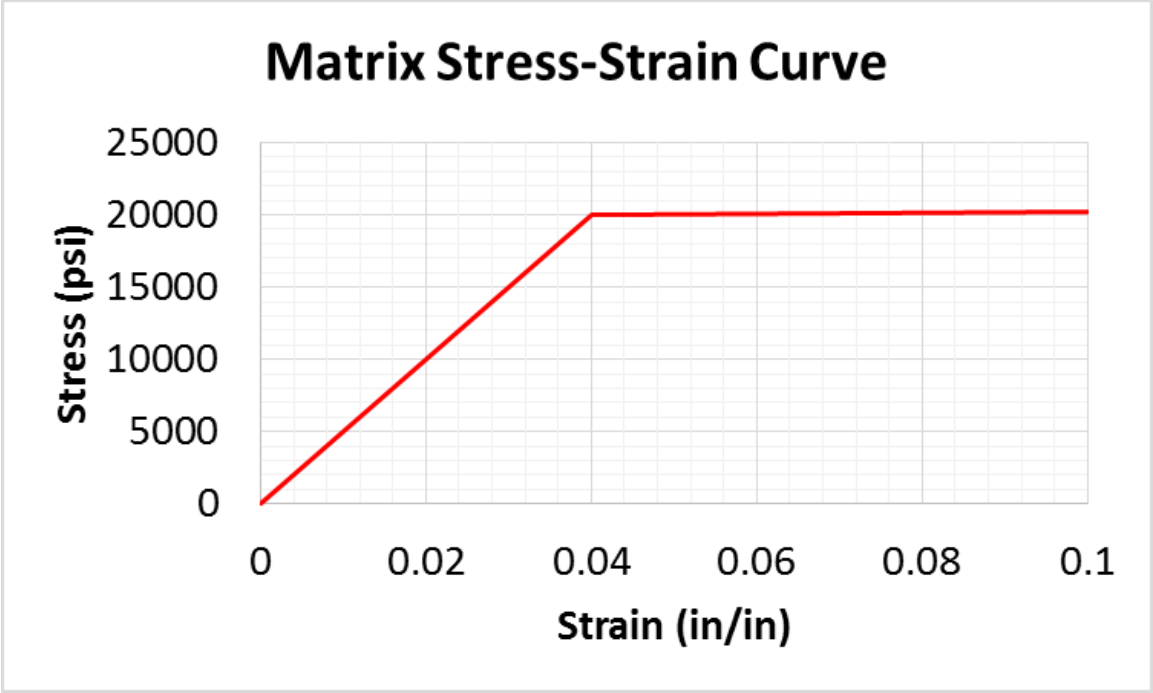

Figure 4.1 Assumed Stress vs. Strain Curve for the Matrix

4.2.2 Composite Geometry

The unit cell was determined from the aforementioned Torayca data sheet for the graphite fiber and the assumption of a fiber volume fraction of 54%. The resulting unit cell is repeated as needed for the overall specimen geometry for each test. For the available WSU tests, the VTSS specimen geometries were identical to the experimental geometries, which were as follows.

4.2.2.1 Tension Tests

Because of the formulation of the VTSS, it is only necessary to model the gage length, which was 2 in. with a width of 0.5 in for the tension tests. These dimensions were based on ASTM D 3039 (D30 Committee, 2014). The layup consisted of two plies ($[0°]_2$ stacking sequence).

4.2.2.2 Compression Tests

The specimen geometry for the compression tests was dictated by the requirement of a Split-Hopkinson Pressure Bar (SHPB) apparatus that the specimen reach equilibrium at an early stage during the test. With this and manufacturing considerations in mind, a 0.25 in. cube was used for the compression tests.

4.2.2.3 Shear Tests

The WSU V-notch rail shear test was completed using a 3 in. by 2.22 in. specimen with a layup consisting of 12 plies ($[0°]_{12}$ stacking sequence). A test case was completed to determine if the inclusion of the notch was necessary for the VTSS shear tests. The geometry for both models, one with a v-notch and one without (labeled 'simple'), is shown in Figure 4.2.

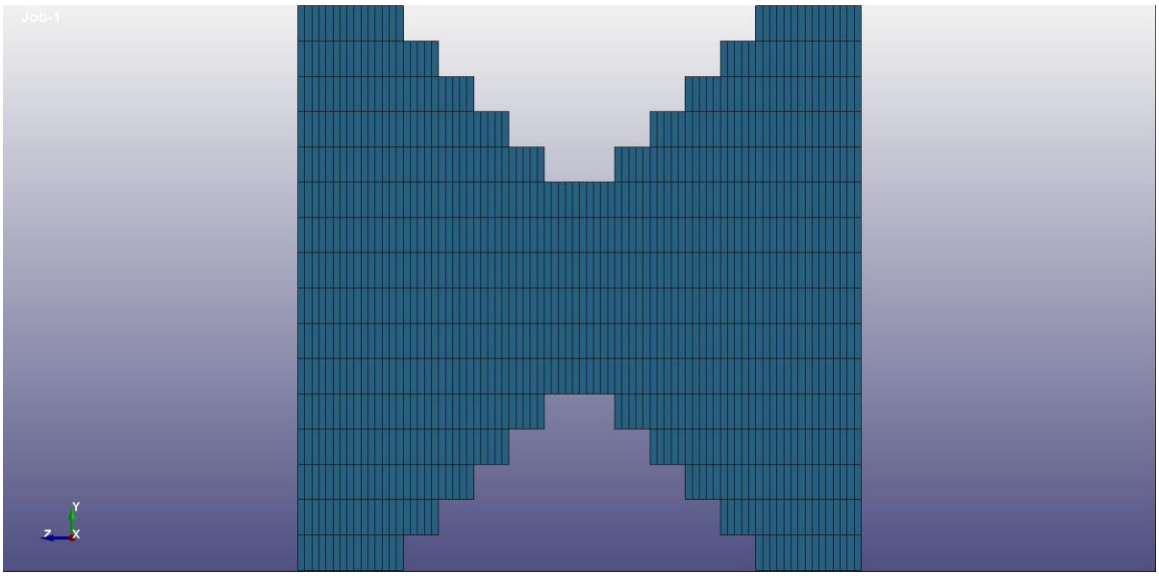

(a)

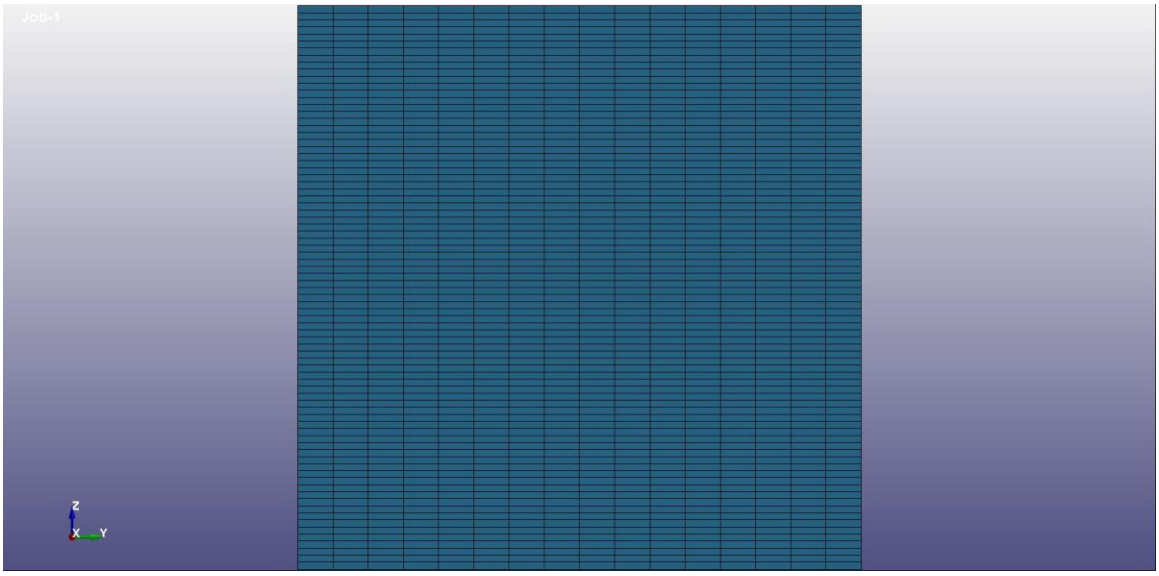

(b)

Figure 4.2 Side View of (a) V-Notch and (b) Simple Geometries for Shear Tests

Using isotropic steel properties for both the fiber and matrix constituents, quasi-static, displacement controlled tests were completed and the results shown in Figure 4.3.

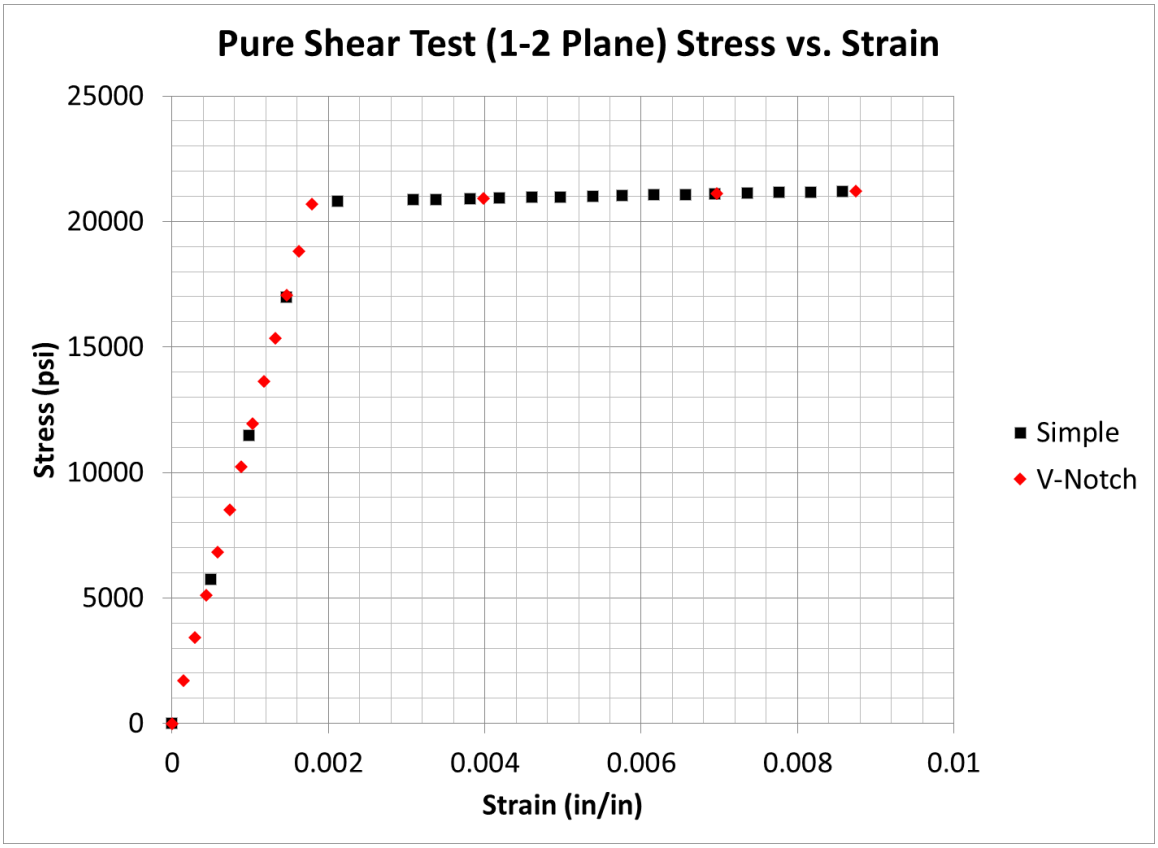

Figure 4.3 Stress vs. Strain $(\tau_{12}$ vs. $\gamma_{12})$

The results show that the geometry has no effect on the results for this test case. Therefore, the VTSS shear tests were completed using specimen without notches.

4.2.2.4 Off-Axis Tests

No experimental data is available for the off-axis tests. For the virtual tests, the specimen dimensions used are the same as those used in the tension tests.

4.2.3 Convergence Study

A convergence study was completed for each test to determine the appropriate meshing parameters. The set of parameters (depicted in Figure 4.4) varied in the study include α, $d_{x\text{-}y}$, and d_z, where

α is the angle of one slice

d_{x-y} is the standard element length in the x-y plane

d_z is the standard element length in the z-direction

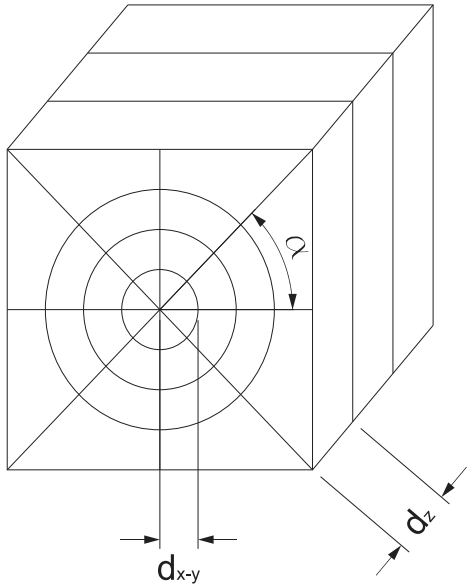

Figure 4.4 Unit Cell Mesh Parameters

Three different sets of parameters (labeled coarse, medium, and fine meshes) were used for the convergence study. Due to the transverse isotropy of the overall composite material, it is unnecessary to complete all 12 tests typically required to characterize an orthotropic material. Only the mesh parameter sets for the necessary tests are shown in Table 4.5.

Table 4.5 Mesh Parameter Sets

Test ID	Coarse Mesh			Medium Mesh			Fine Mesh		
	α (°)	d_{x-y} (in)	d_z (in)	α (°)	d_{x-y} (in)	d_z (in)	α (°)	d_{x-y} (in)	d_z (in)
T1	45	0.008	0.100	22.5	0.004	0.0500	15	0.003	0.033
T2	45	0.008	0.050	22.5	0.004	0.0250	15	0.003	0.017
C1	45	0.008	0.025	22.5	0.004	0.0125	15	0.003	0.008
C2	45	0.008	0.025	22.5	0.004	0.0125	15	0.003	0.008
S12	45	0.008	0.300	22.5	0.008	0.2250	22.5	0.004	0.150
S23	45	0.008	0.300	22.5	0.008	0.2250	22.5	0.004	0.150
O12	45	0.008	0.100	22.5	0.004	0.0500	15	0.003	0.033
O23	45	0.008	0.025	45	0.008	0.0100	22.5	0.008	0.010

Information on the resulting model sizes is summarized in Table 4.6, which includes the number of nodes, elements, and degrees of freedom (DOFs) comprising each model.

Table 4.6 Mesh Size Information

Test ID	Coarse Mesh		
	Nodes	Elements	DOFs
T1	12,453	13,440	37,359
T2	25,003	25,920	75,009
C1	11,099	11,760	33,297
C2	11,099	11,760	33,297
S12	159,995	172,800	479,985
S23	159,995	172,800	479,985
O12	35,557	35,564	106,671
O23	141,696	124,500	425,088
Test ID	Medium Mesh		
	Nodes	Elements	DOFs
T1	85,321	89,600	255,963
T2	204,309	207,360	612,927
C1	91,749	94,080	275,247
C2	91,749	94,080	275,247
S12	436,335	483,840	1,309,005
S23	436,335	483,840	1,309,005
O12	219,802	220,744	659,406
O23	318,816	332,000	956,448
Test ID	Fine Mesh		
	Nodes	Elements	DOFs
T1	276,830	286,944	830,490
T2	532,735	544,320	1,598,205
C1	247,328	255,192	741,984
C2	247,328	255,192	741,984
S12	1,336,629	1,382,400	4,009,887
S23	1,336,629	1,382,400	4,009,887
O12	670,692	672,976	2,012,076
O23	631,548	660,960	1,894,644

Convergence is established with the fine models, shown in Appendix B. Only the fine mesh results (labeled ‘VTSS’) are used to compare against available computed and experimental data in the following section.

4.2.4 Test Details and Results

The finite element models were analyzed using both LS-DYNA© and ABAQUS©. However, the results were nearly identical from each FE software package. Therefore, only one data set is included for the FE results, labeled 'VTSS'.

4.2.4.1 Tension Test – 1-Direction

A displacement controlled analysis is carried out. Displacements are applied to the nodes on the opposite face (to the supported face) in the 1-direction in ten equal steps of 0.004 in starting with an initial displacement of 0.004 in. The resulting applied displacement in the final step, 0.04 in, is used to produce a similar total strain as the available computed and experimental data.

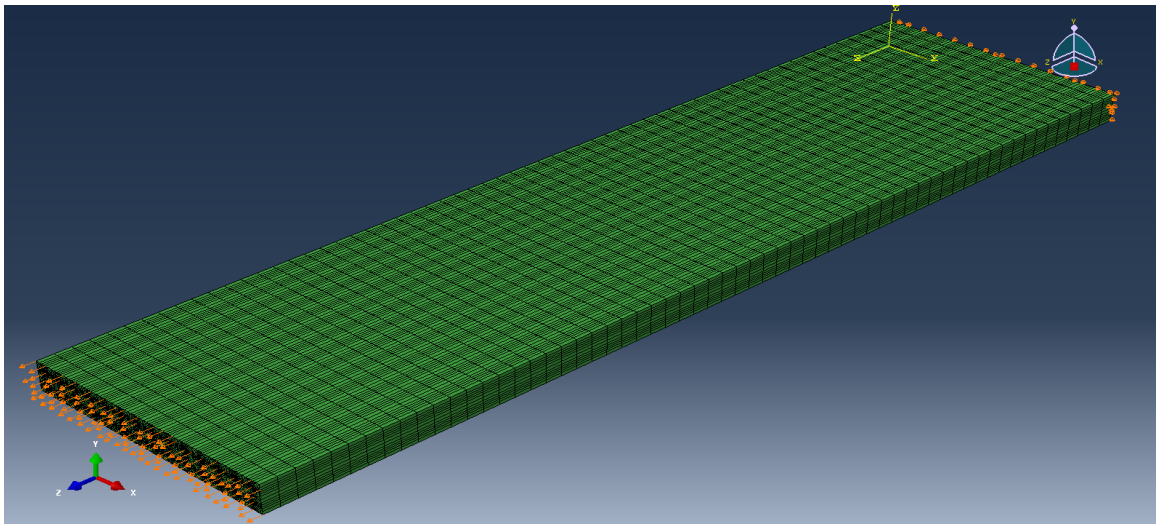

Figure 4.5 Boundary Conditions for Tension Test (1-Direction)

The test details and results for the fine mesh are discussed below.

Table 4.7 Model Parameters

Parameter	Value
a	0.03737 in
r_{fiber}	0.01549 in
L	0.4 in
n_{rows}	1
$n_{columns}$	4

Table 4.8 Model Size Information

Category for entire model	Value
Total number of nodes	276,830
Total number of elements	286,944
Number of C3D6 elements in fiber	40,992
Number of C3D8 elements in fiber	163,968
Number of C3D8 elements in matrix	81,984

The elements used in generating the homogenized material properties for the test are shown in red in Figure 4.6.

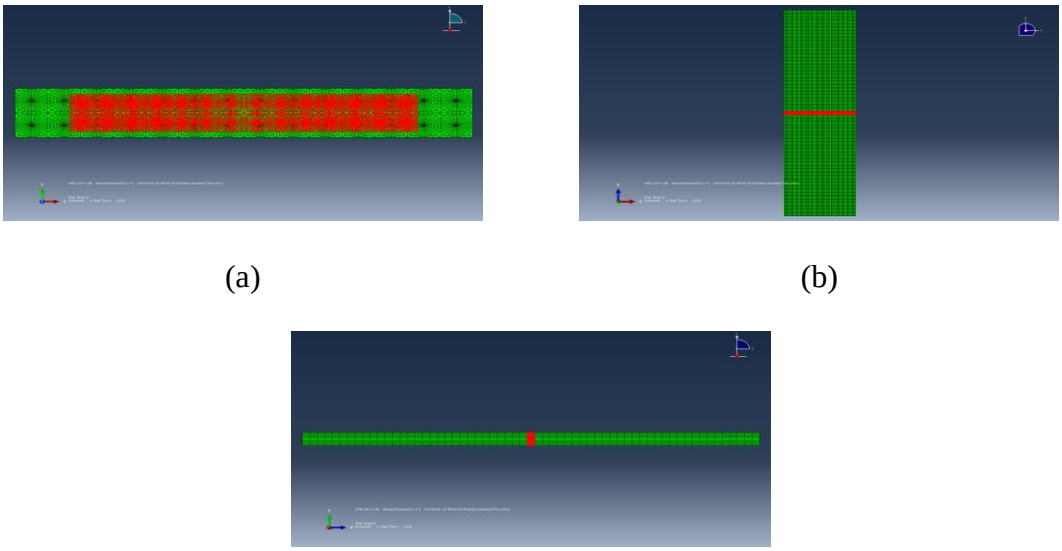

(a) (b)

(c)

Figure 4.6 Section View of (a) x-y (b) x-z and (c) z-y Planes of the Elements used in Computing the Homogenized Material Properties

The homogenized engineering stress-strain curve is plotted along with the available computed and experimental data in Figure 4.7.

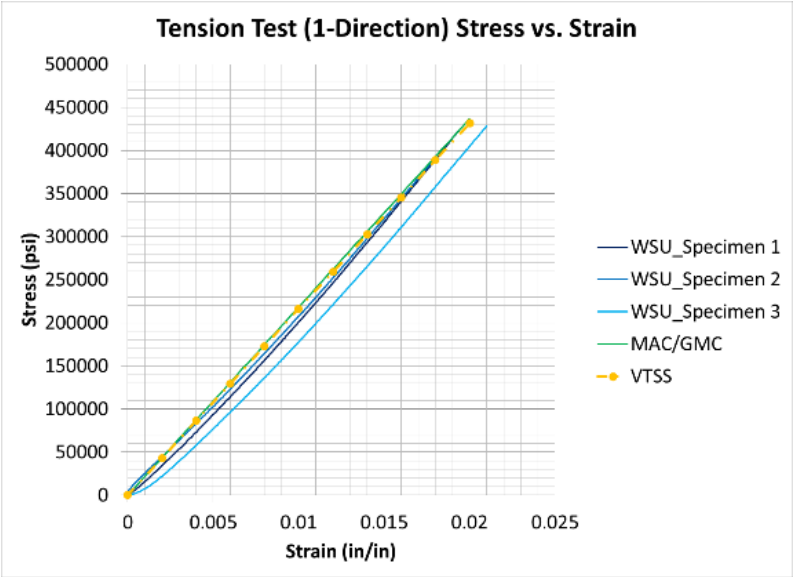

Figure 4.7 Stress vs. Strain $(\sigma_{11}$ vs. $\varepsilon_{11})$

The stress (σ_{11}) distribution plotted on the deformed shape of the final step of analysis is shown in Figure 4.8.

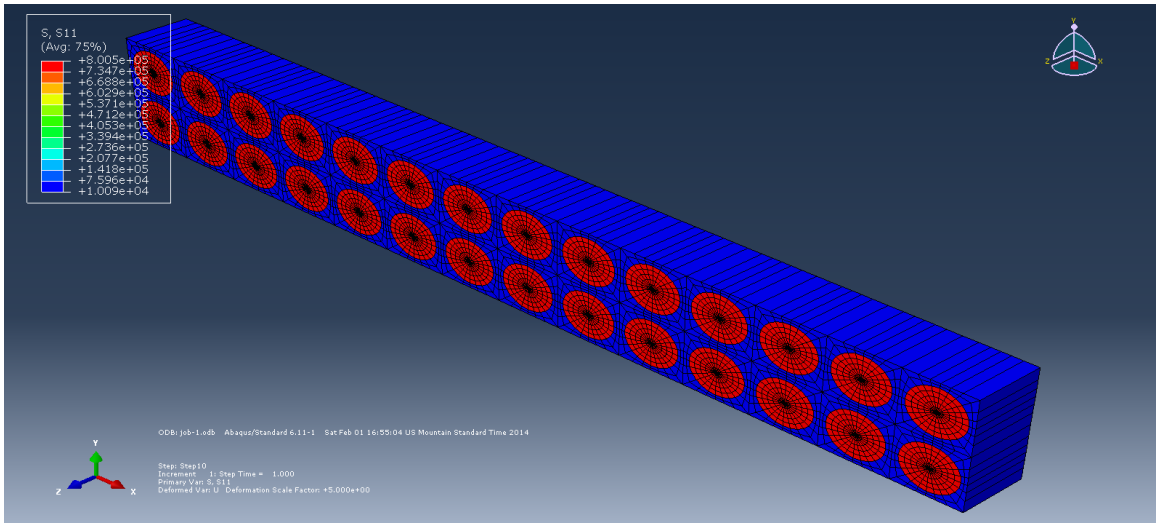

Figure 4.8 Stress (σ_{11}) Distribution in the Post-Processed Region

The strain (ε_{11}) distribution plotted on the deformed shape of the final step of analysis is shown in Figure 4.9.

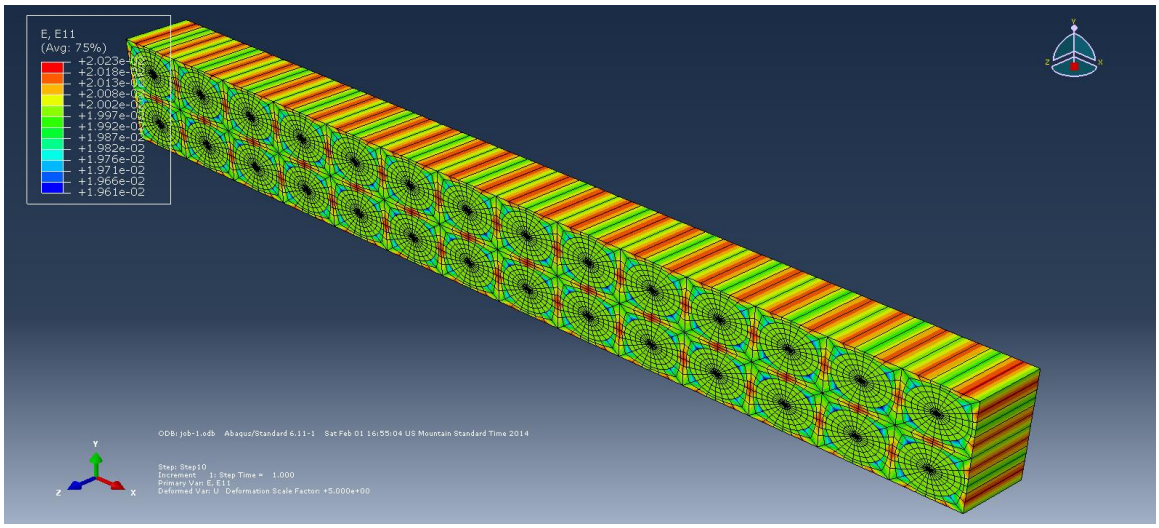

Figure 4.9 Strain (ε_{11}) Distribution in the Post-Processed Region

4.2.4.2 Tension Test – 2-Direction

A displacement controlled analysis is carried out. Displacements are applied to the nodes on the opposite face (to the supported face) in the 2-direction in ten equal steps of 0.006 in starting with an initial displacement of 0.006 in. The resulting applied displacement in the final step, 0.06 in, is used to produce a similar total strain as the available computed and experimental data.

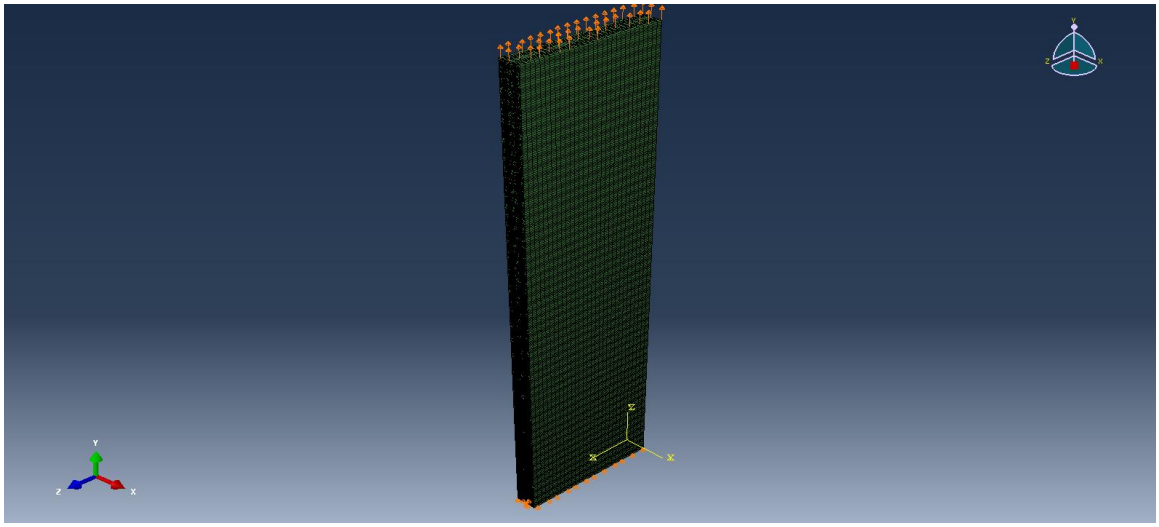

Figure 4.10 Boundary Conditions for Tension Test (2-Direction)

The test details and results for the fine mesh are discussed below.

Table 4.9 Model Parameters

Parameter	Value
a	0.03737 in
r_{fiber}	0.01549 in
L	0.1 in
n_{rows}	10
$n_{columns}$	1

Table 4.10 Model Size Information

Category for entire model	Value
Total number of nodes	2,079,385
Total number of elements	2,177,280
Number of C3D6 elements in fiber	311,040
Number of C3D8 elements in fiber	1,244,160
Number of C3D8 elements in matrix	622,080

The elements used in generating the homogenized material properties for the test are shown in red in Figure 4.11.

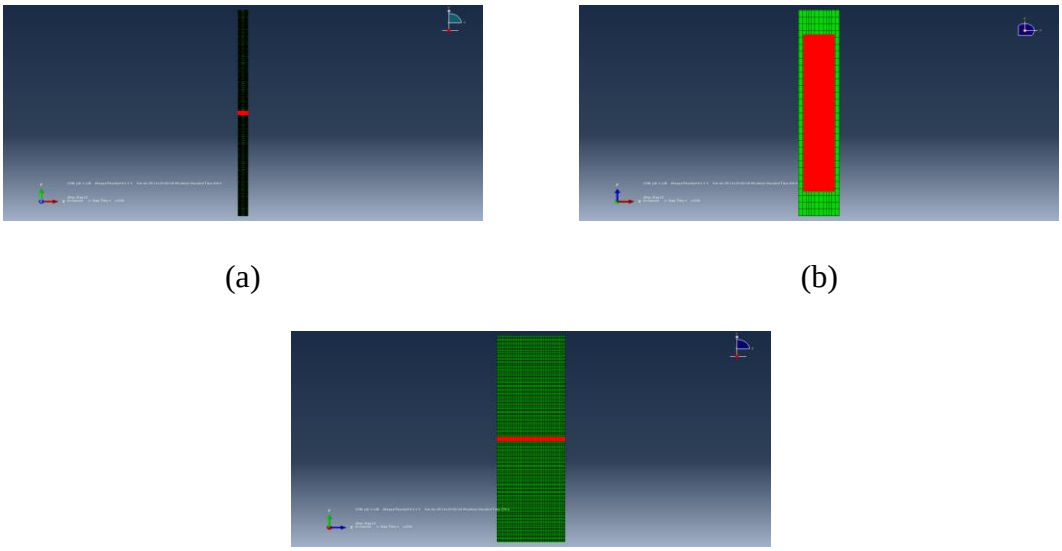

(a) (b)

(c)

Figure 4.11 Section View of (a) x-y (b) x-z and (c) z-y Planes of the Elements used in Computing the Homogenized Material Properties

The homogenized engineering stress-strain curve is plotted along with the available computed data in Figure 4.12.

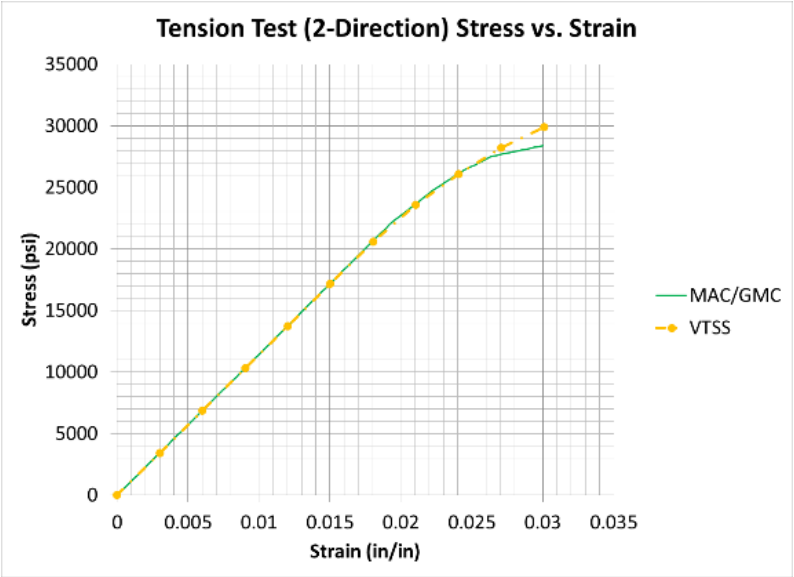

Figure 4.12 Stress vs. Strain $(\sigma_{22}$ vs. $\varepsilon_{22})$

The stress (σ_{22}) distribution plotted on the deformed shape of the final step of analysis is shown in Figure 4.13.

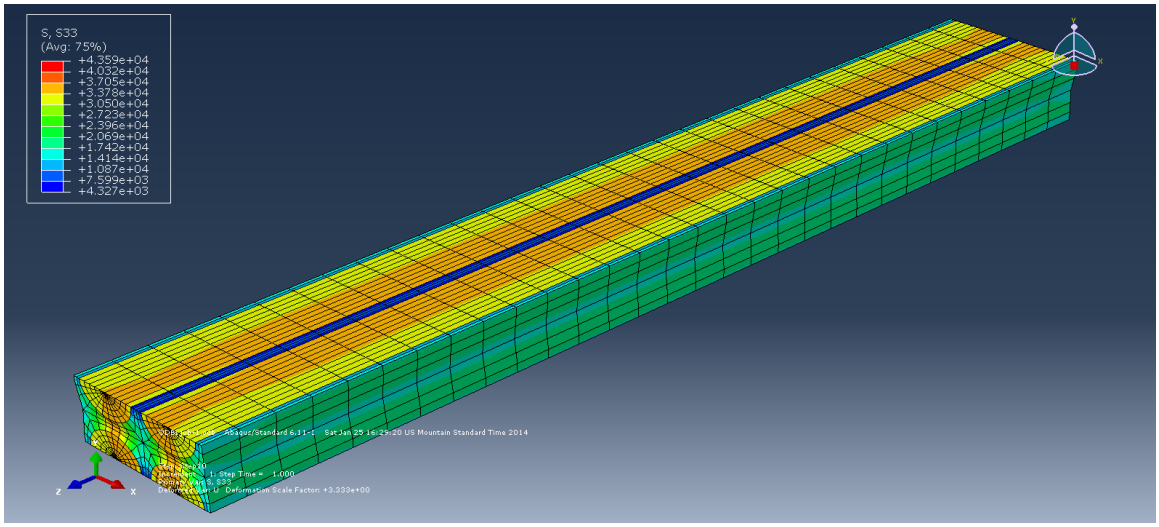

Figure 4.13 Stress (σ_{22}) Distribution in the Post-Processed Region

The strain (ε_{22}) distribution plotted on the deformed shape of the final step of analysis is shown in Figure 4.14.

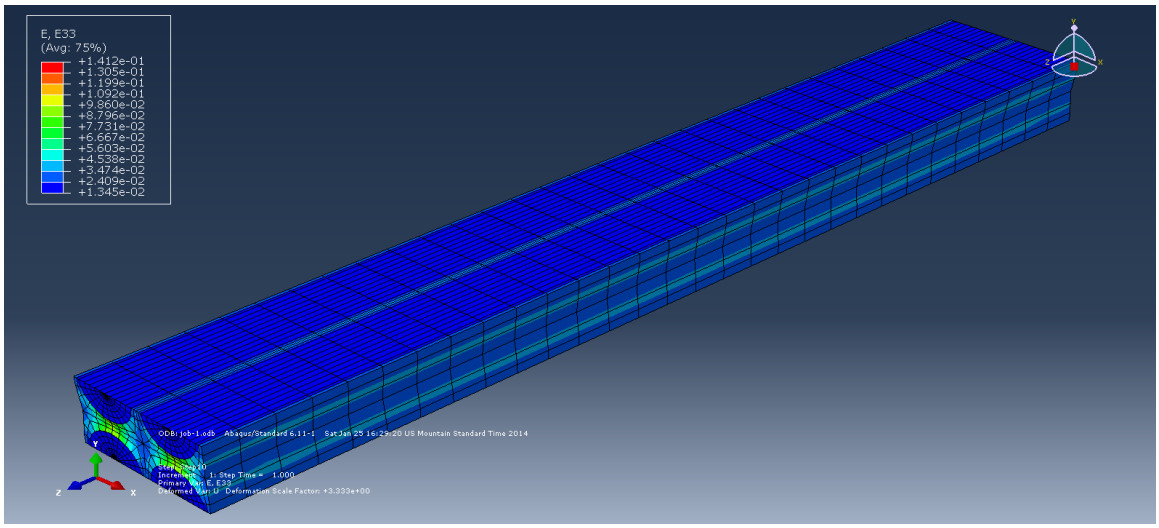

Figure 4.14 Strain (ε_{22}) Distribution in the Post-Processed Region

4.2.4.3 Tension Test – 3-Direction

This test is not necessary because of the transverse isotropy of the composite material (same as the tension in the 2-direction test).

4.2.4.4 Compression Test – 1-Direction

A displacement controlled analysis is carried out. Displacements are applied to the nodes on the opposite face (to the supported face) in the 1-direction in ten equal steps of 0.0005 in starting with an initial displacement of 0.0005 in. The resulting applied displacement in the final step, 0.005 in, is used to produce a similar total strain as the available computed and experimental data for the tension test in the same direction.

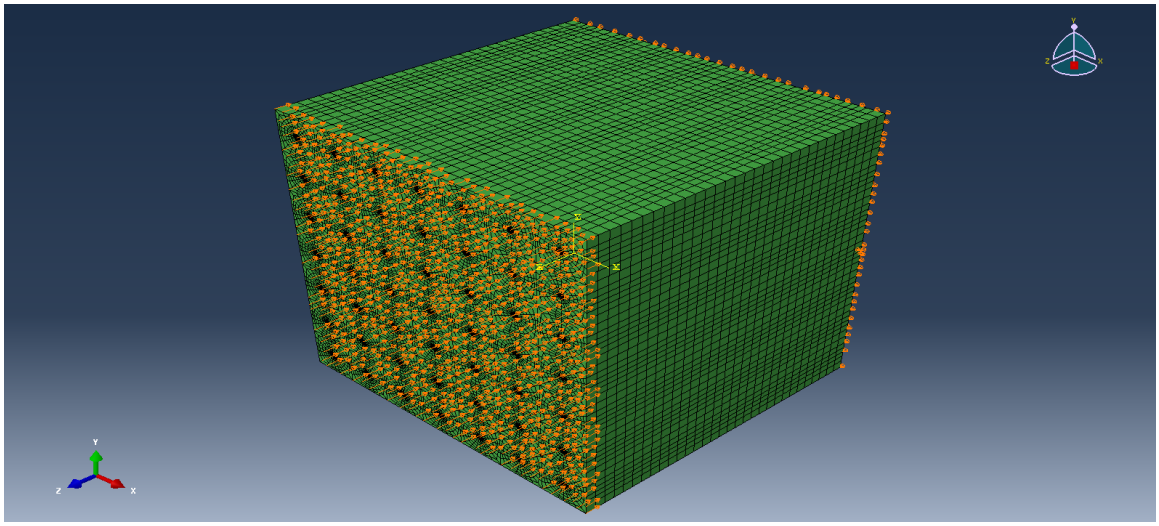

Figure 4.15 Boundary Conditions for Compression Test (1-Direction)

The test details and results for the fine mesh are discussed below.

Table 4.11 Model Parameters

Parameter	Value
a	0.03737 in
r_{fiber}	0.01549 in
L	0.25 in
n_{rows}	7
$n_{columns}$	7

Table 4.12 Model Size Information

Category for entire model	Value
Total number of nodes	247,328
Total number of elements	255,192
Number of C3D6 elements in fiber	36,456
Number of C3D8 elements in fiber	145,824
Number of C3D8 elements in matrix	72,912

The elements used in generating the homogenized material properties for the test are shown in red in Figure 4.16.

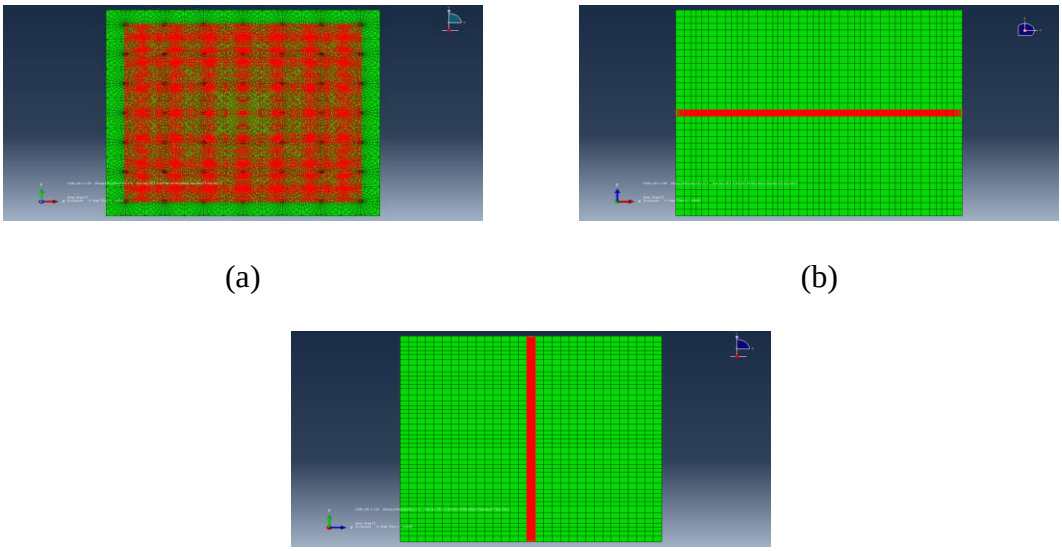

(a) (b)

(c)

Figure 4.16 Section View of (a) x-y (b) x-z and (c) z-y Planes of the Elements used in Computing the Homogenized Material Properties

The homogenized engineering stress-strain curve is plotted along with the available computed data in Figure 4.17.

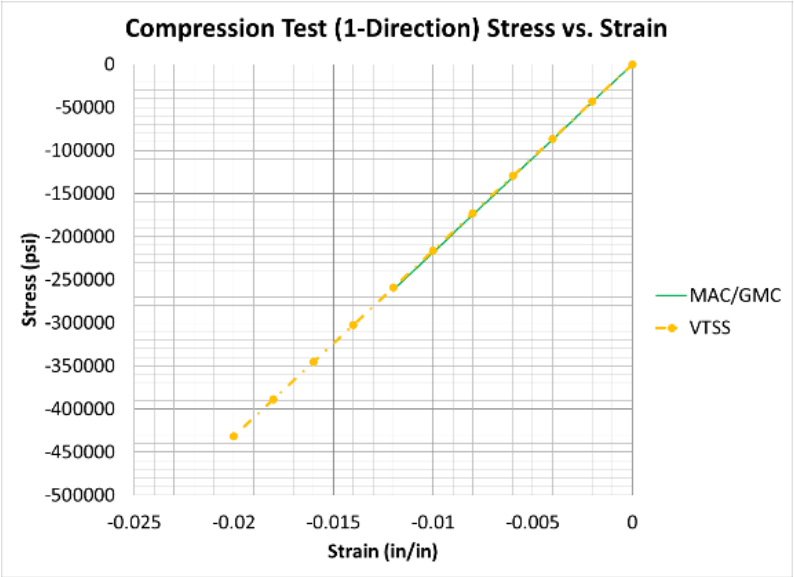

Figure 4.17 Stress vs. Strain $(\sigma_{11}$ vs. $\varepsilon_{11})$

The stress (σ_{11}) distribution plotted on the deformed shape of the final step of analysis is shown in Figure 4.18.

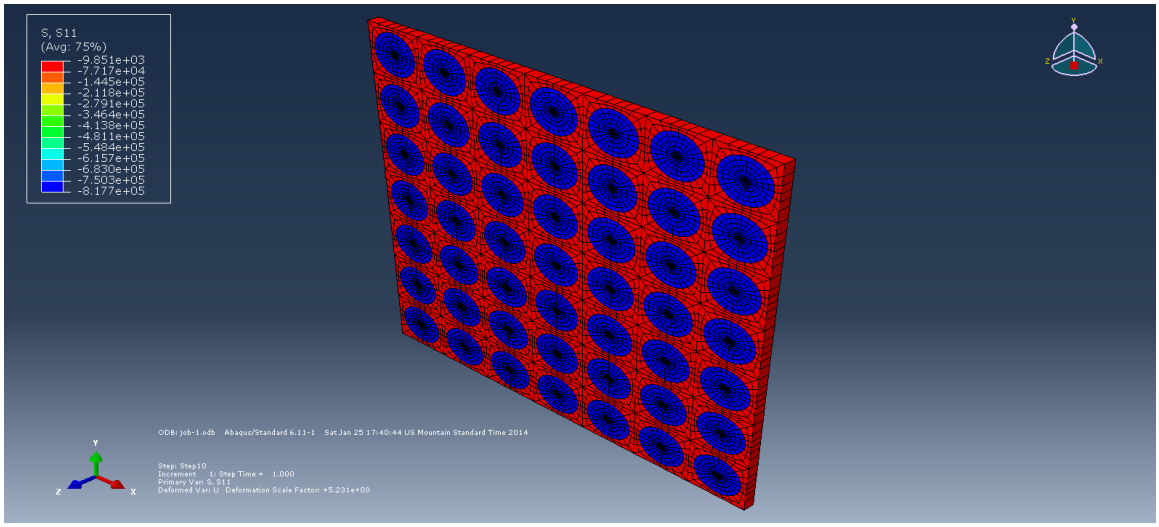

Figure 4.18 Stress (σ_{11}) Distribution in the Post-Processed Region

The strain (ε_{11}) distribution plotted on the deformed shape of the final step of analysis is shown in Figure 4.19.

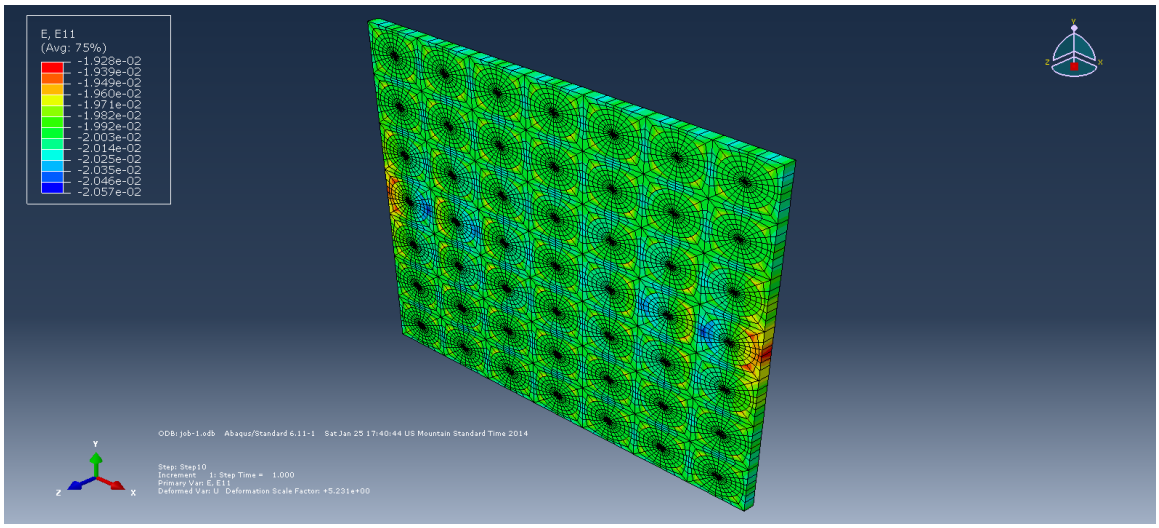

Figure 4.19 Strain (ε_{11}) Distribution in the Post-Processed Region

4.2.4.5 Compression Test – 2-Direction

A displacement controlled analysis is carried out. Displacements are applied to the nodes on the opposite face (to the supported face) in the 2-direction in ten equal steps of 0.00075 in starting with an initial displacement of 0.00075 in. The resulting applied displacement in the final step, 0.0075 in is used to produce a similar total strain as the available computed and experimental data for the tension test in the same direction.

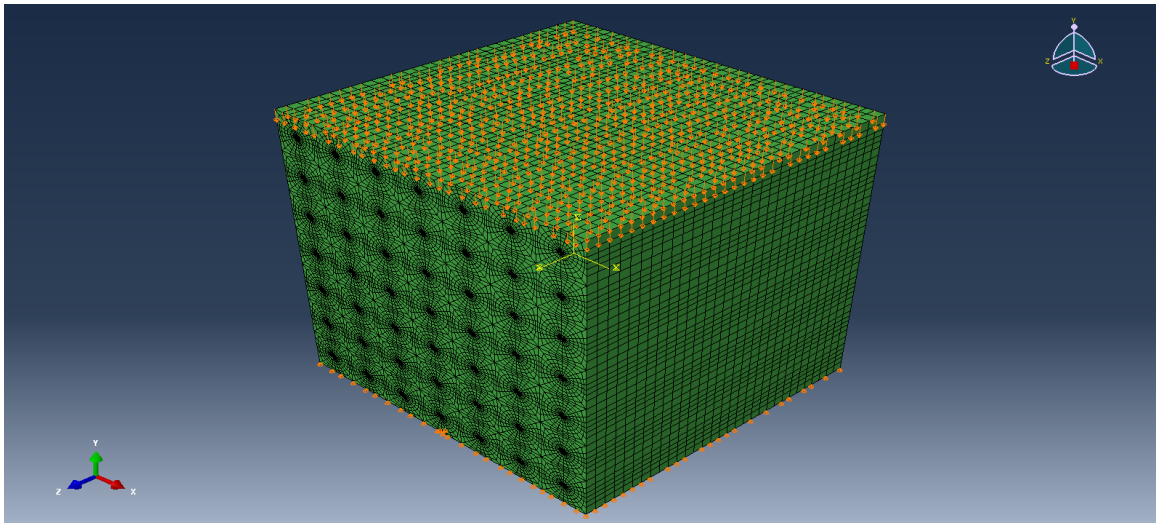

Figure 4.20 Boundary Conditions for Compression Test (2-Direction)

The test details and results for the fine mesh are discussed below.

Table 4.13 Model Parameters

Parameter	Value
a	0.03737 in
r_{fiber}	0.01549 in
L	0.25 in
n_{rows}	7
$n_{columns}$	7

Table 4.14 Model Size Information

Category for entire model	Value
Total number of nodes	247,328
Total number of elements	255,192
Number of C3D6 elements in fiber	36,456
Number of C3D8 elements in fiber	145,824
Number of C3D8 elements in matrix	72,912

The elements used in generating the homogenized material properties for the test are shown in red in Figure 4.21.

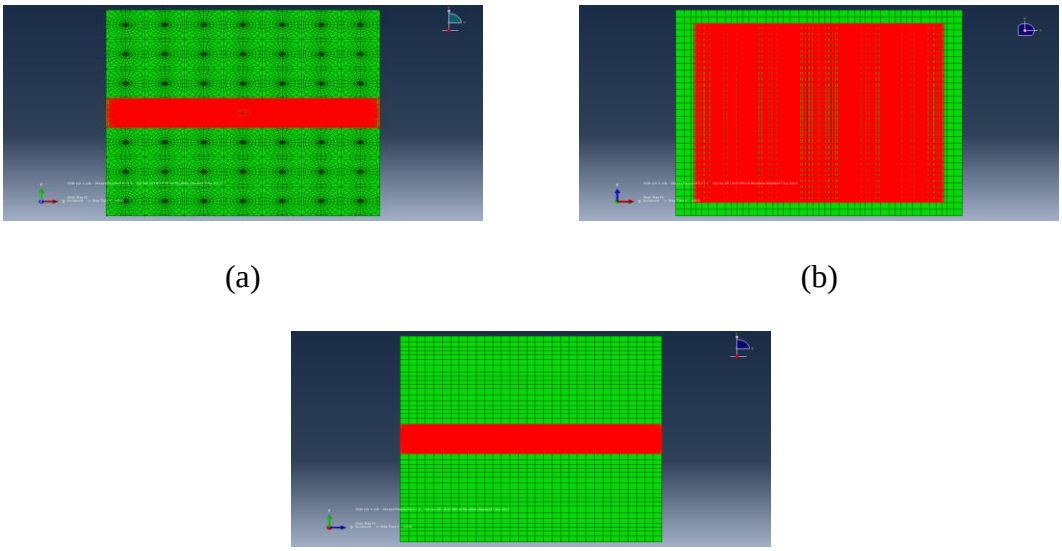

(a) (b)

(c)

Figure 4.21 Section View of (a) x-y (b) x-z and (c) z-y Planes of the Elements used in Computing the Homogenized Material Properties

The homogenized engineering stress-strain curve is plotted along with the available computed data in Figure 4.22.

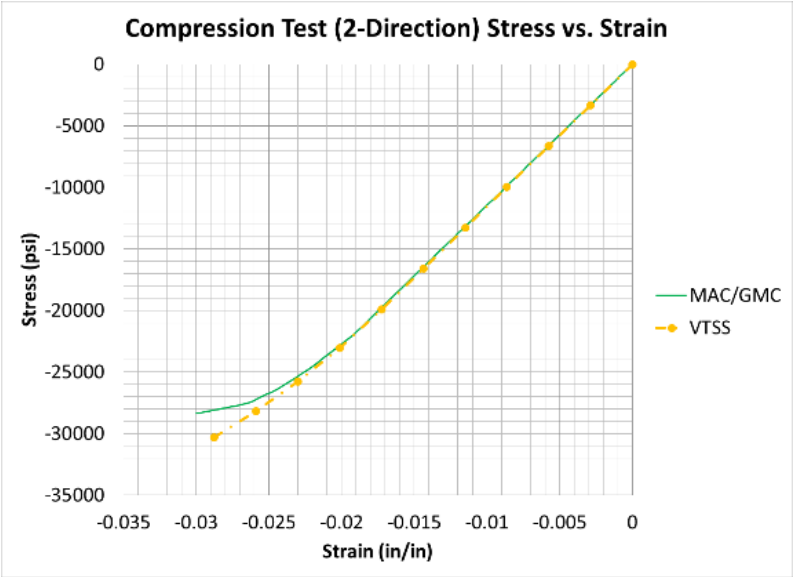

Figure 4.22 Stress vs. Strain $(\sigma_{22}$ vs. $\varepsilon_{22})$

The stress (σ_{22}) distribution plotted on the deformed shape of the final step of analysis is shown in Figure 4.23.

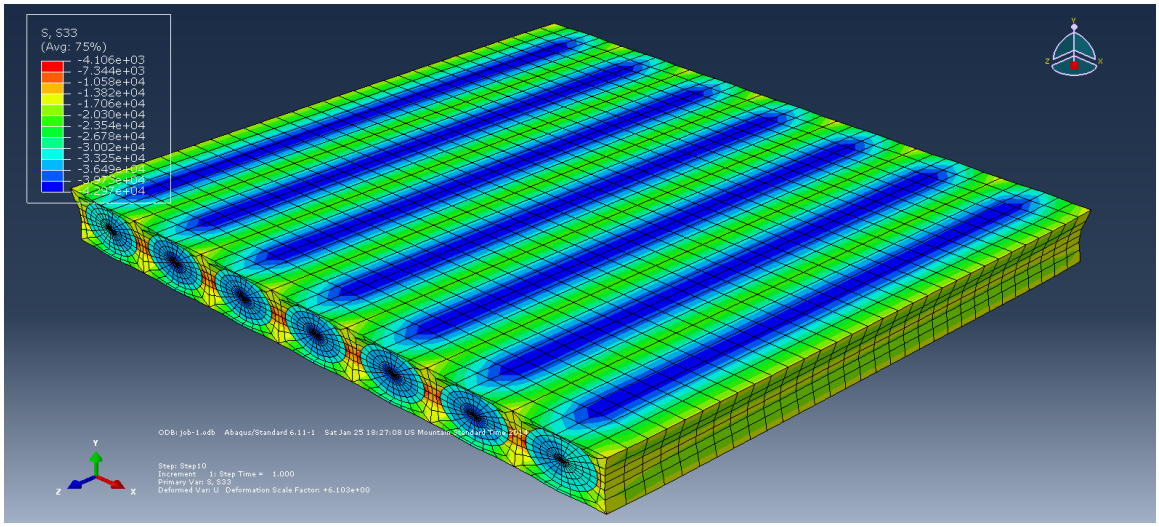

Figure 4.23 Stress (σ_{22}) Distribution in the Post-Processed Region

The strain (ε_{22}) distribution plotted on the deformed shape of the final step of analysis is shown in Figure 4.24.

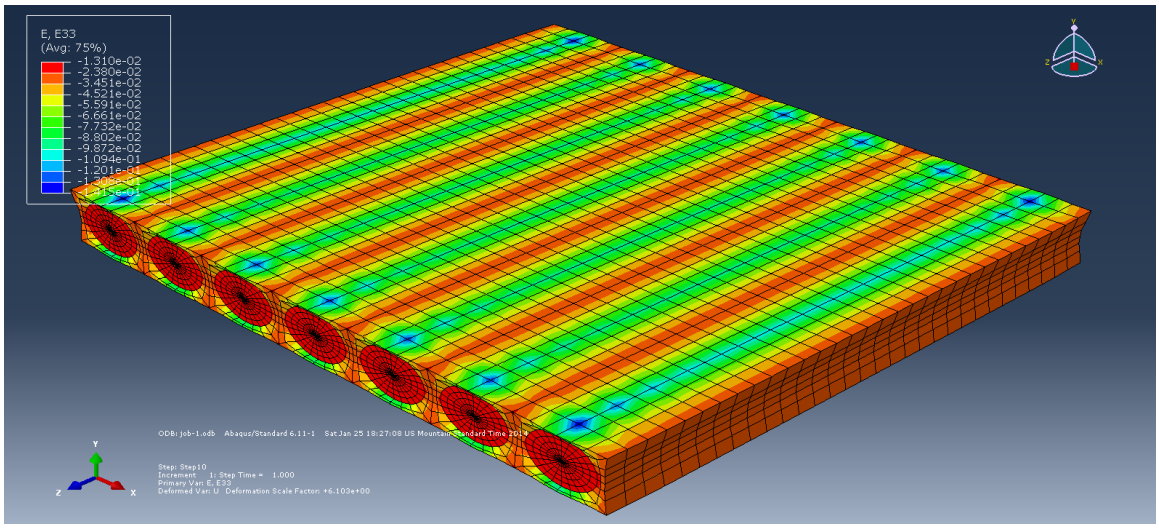

Figure 4.24 Strain (ε_{22}) Distribution in the Post-Processed Region

4.2.4.6 Compression Test – 3-Direction

This test is not necessary because of the transverse isotropy of the composite material (same as the compression in the 2-direction test).

4.2.4.7 Pure Shear Test – 1-2 Plane

A displacement controlled analysis is carried out. Displacements are applied to the nodes on the top face in the 1-direction in twenty equal steps of 0.01 in starting with an initial displacement of 0.00002 in. The resulting applied displacement in the final step, 0.2 in, is used to produce a similar total strain as the available computed and experimental data.

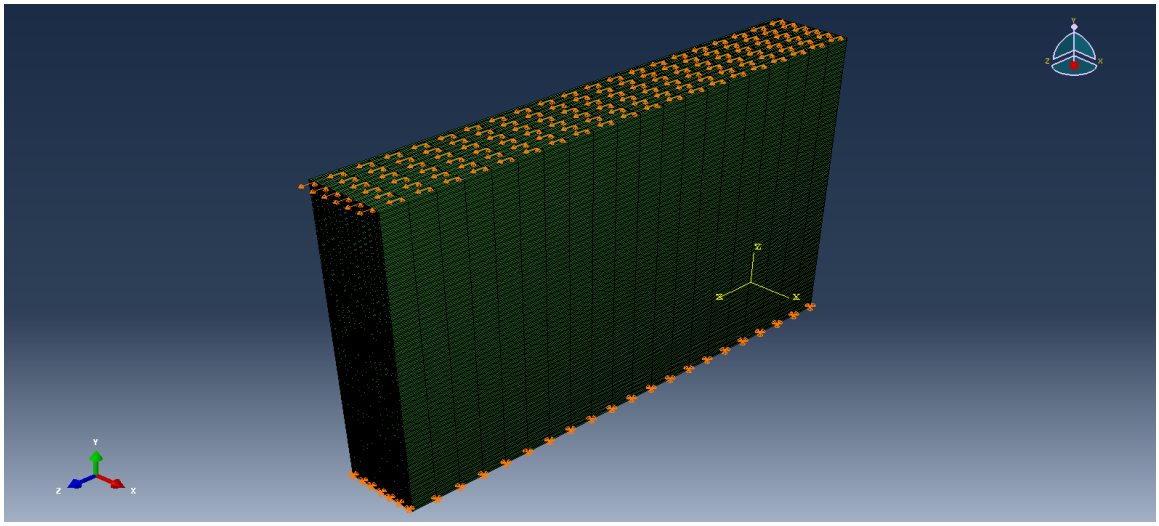

Figure 4.25 Boundary Conditions for Pure Shear Test (1-2 Plane)

The test details and results for the fine mesh are discussed below.

Table 4.15 Model Parameters

Parameter	Value
a	0.03737 in
r_{fiber}	0.01549 in
L	3.0 in
n_{rows}	60
$n_{columns}$	12

Table 4.16 Model Size Information

Category for entire model	Value
Total number of nodes	1,336,629
Total number of elements	1,382,400
Number of C3D6 elements in fiber	230,400
Number of C3D8 elements in fiber	921,600
Number of C3D8 elements in matrix	230,400

The elements used in generating the homogenized material properties for the test are shown in red in Figure 4.26.

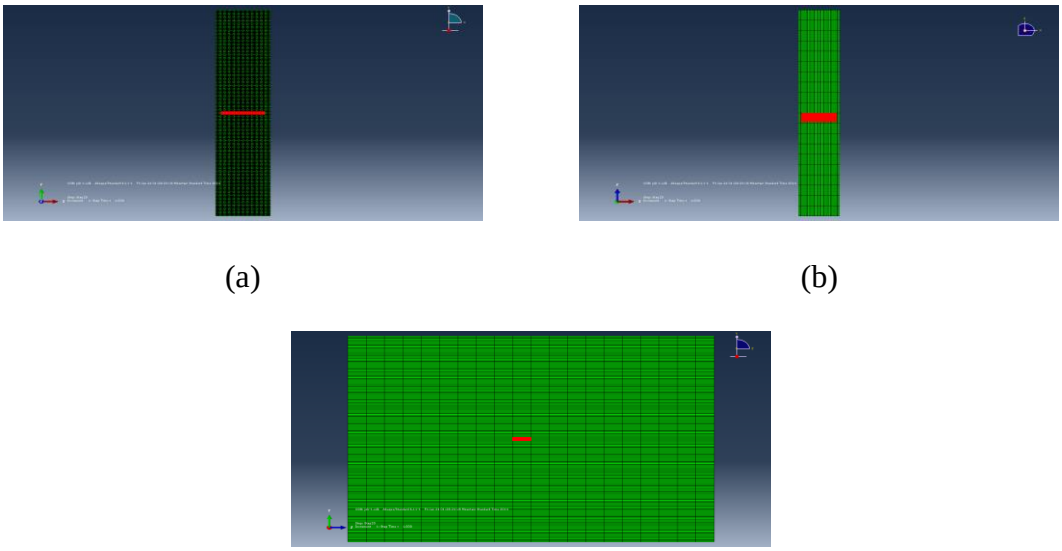

(a) (b)

(c)

Figure 4.26 Section View of (a) x-y (b) x-z and (c) z-y Planes of the Elements used in Computing the Homogenized Material Properties

The homogenized engineering stress-strain curve is plotted along with the available computed and experimental data in Figure 4.27.

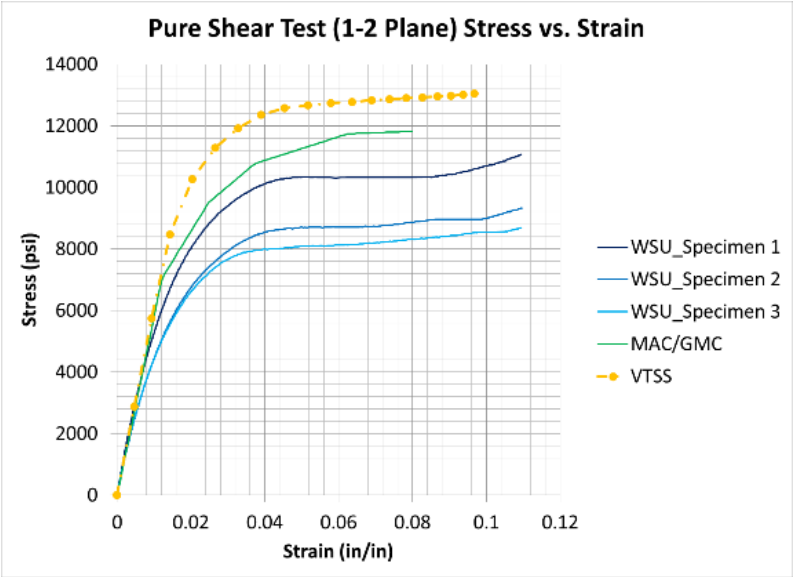

Figure 4.27 Stress vs. Strain $(\tau_{12}$ vs. $\gamma_{12})$

The stress (τ_{12}) distribution plotted on the deformed shape of the final step of analysis is shown in Figure 4.28.

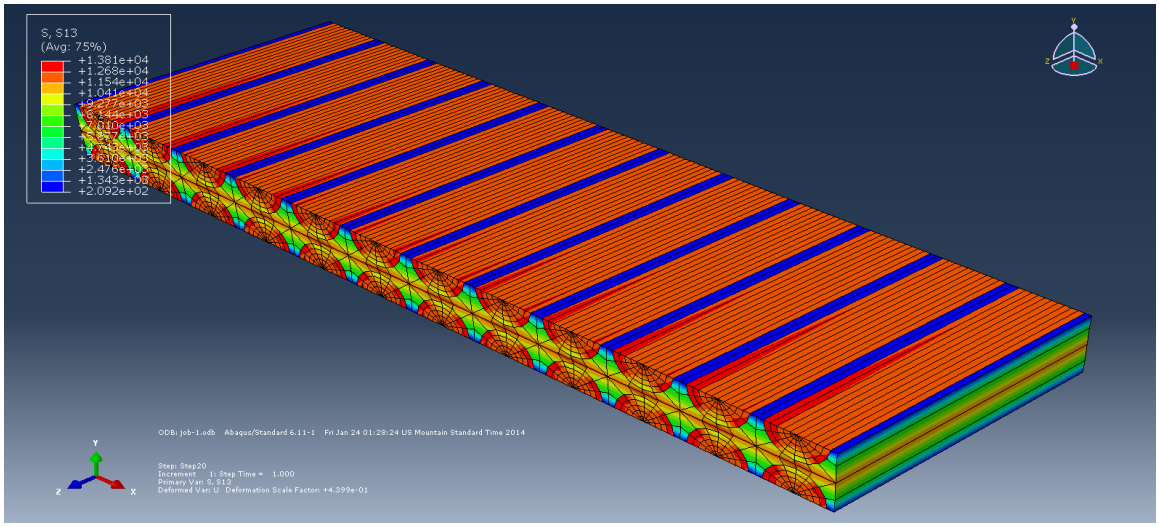

Figure 4.28 Stress (τ_{12}) Distribution in the Post-Processed Region

The strain (γ_{12}) distribution plotted on the deformed shape of the final step of analysis is shown in Figure 4.29.

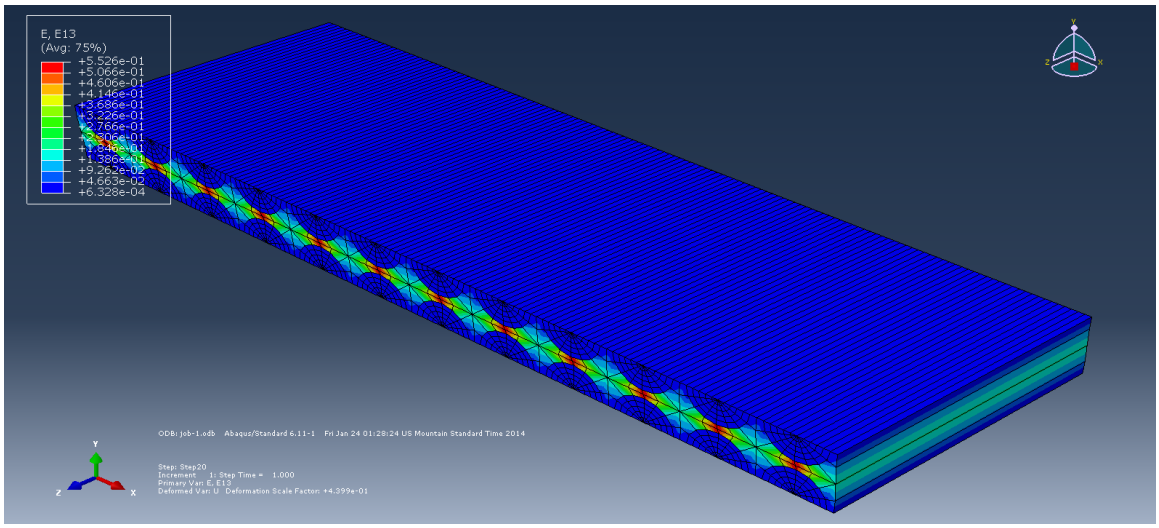

Figure 4.29 Strain (γ_{12}) Distribution in the Post-Processed Region

4.2.4.8 Pure Shear Test – 2-3 Plane

A displacement controlled analysis is carried out. Displacements are applied to the nodes on the left face in the 2-direction in twenty equal steps of 0.0018 in starting with an initial displacement of 0.000034 in. The resulting applied displacement in the final step, 0.034 in, is used to produce a similar total strain as the available computed data.

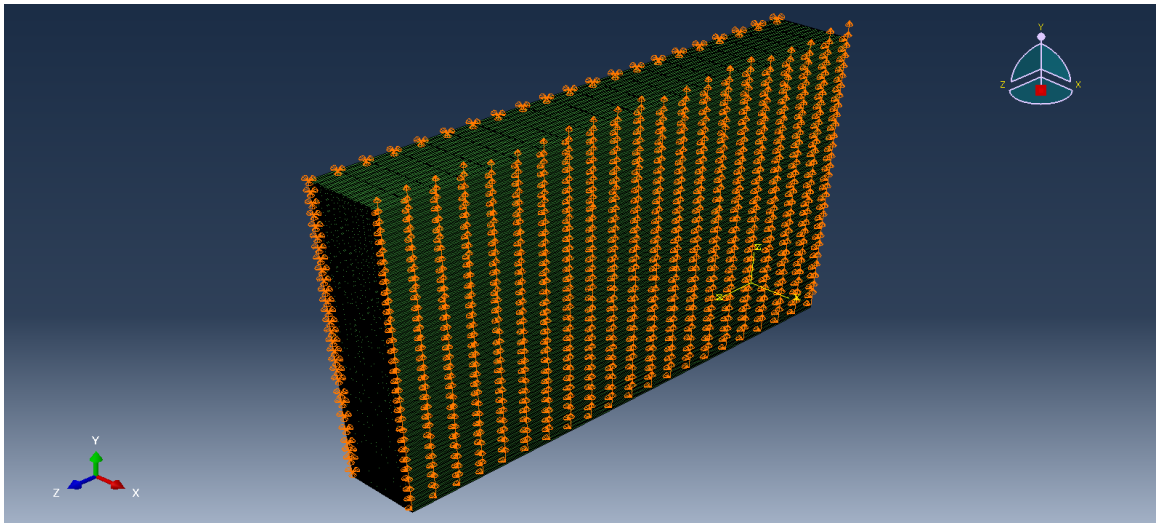

Figure 4.30 Boundary Conditions for Pure Shear Test (2-3 Plane)

The test details and results for the fine mesh are discussed below.

Table 4.17 Model Parameters

Parameter	Value
a	0.03737 in
r_{fiber}	0.01549 in
L	3.0 in
n_{rows}	60
$n_{columns}$	12

Table 4.18 Model Size Information

Category for entire model	Value
Total number of nodes	1,336,629
Total number of elements	1,382,400
Number of C3D6 elements in fiber	230,400
Number of C3D8 elements in fiber	921,600
Number of C3D8 elements in matrix	230,400

The elements used in generating the homogenized material properties for the test are shown in red in Figure 4.31.

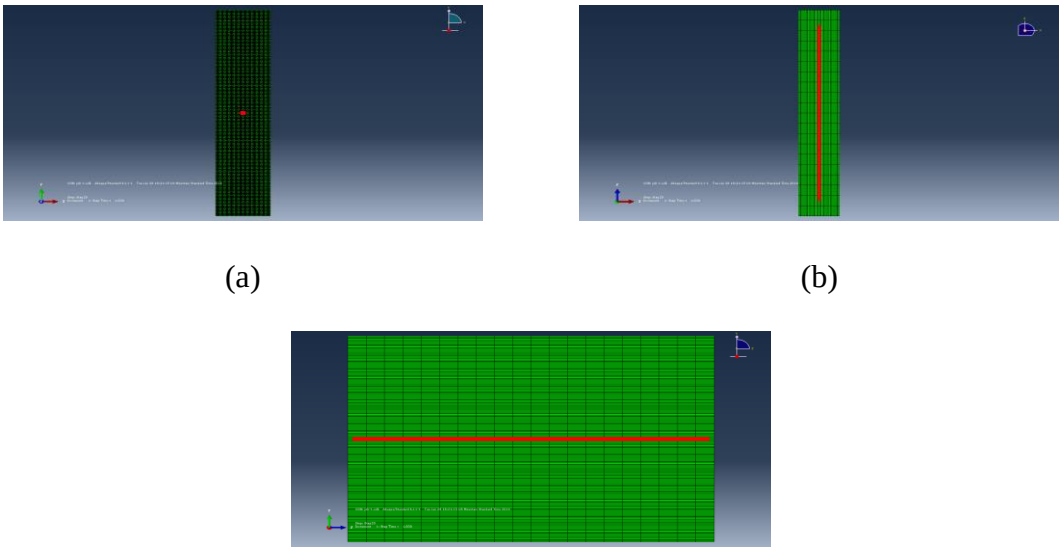

(a) (b)

(c)

Figure 4.31 Section View of (a) x-y (b) x-z and (c) z-y Planes of the Elements used in Computing the Homogenized Material Properties

The homogenized engineering stress-strain curve is plotted along with the available computed data in Figure 4.32.

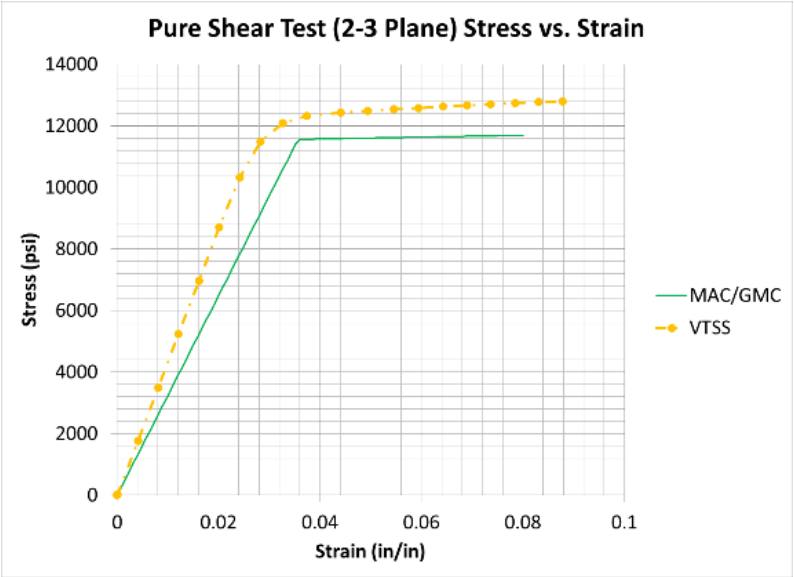

Figure 4.32 Stress vs. Strain $(\tau_{23}$ vs. $\gamma_{23})$

The stress (τ_{23}) distribution plotted on the deformed shape of the final step of analysis is shown in Figure 4.33.

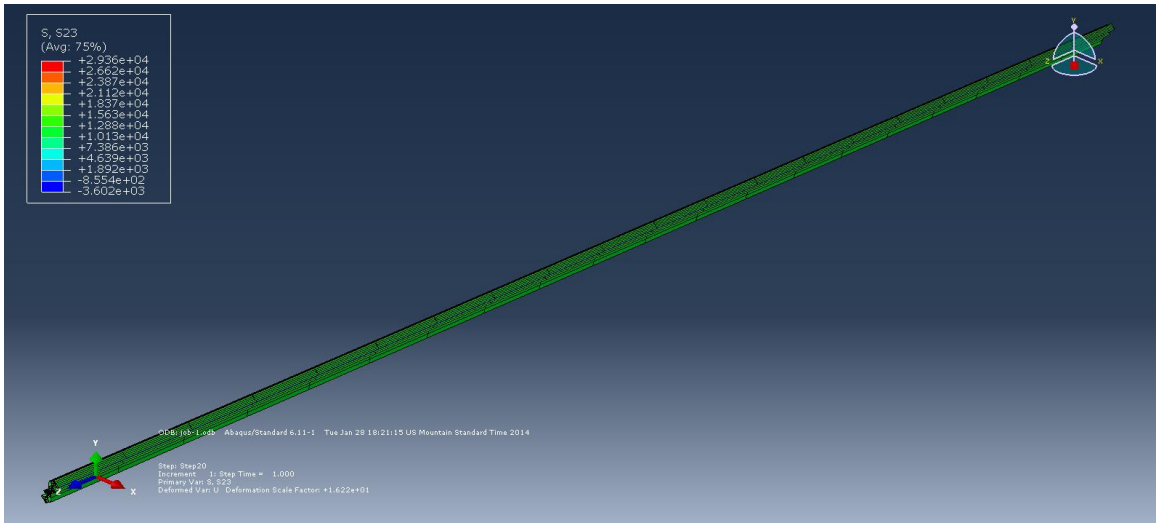

Figure 4.33 Stress (τ_{23}) Distribution in the Post-Processed Region

The strain (γ_{23}) distribution plotted on the deformed shape of the final step of analysis is shown in Figure 4.34.

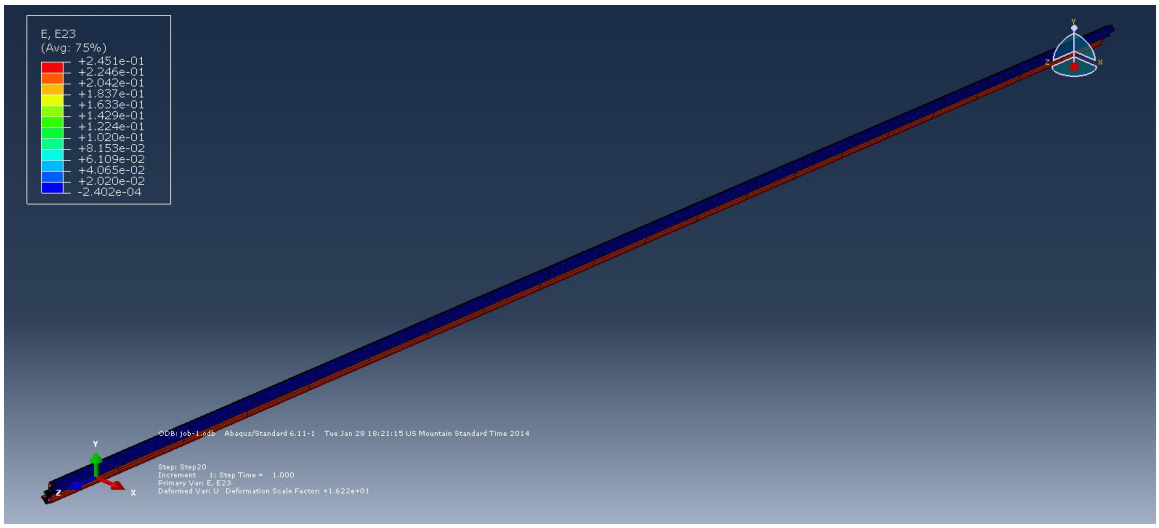

Figure 4.34 Strain (γ_{23}) Distribution in the Post-Processed Region

4.2.4.9 Pure Shear Test – 1-3 Plane

This test is not necessary because of the transverse isotropy of the composite material (same as the pure shear in the 1-2 plane test).

4.2.4.10 Off-Axis Test – 45°, 1-2 Plane

A displacement controlled analysis is carried out. Displacements are applied to the nodes in the displacement section in the test direction (45°) in ten equal steps of 0.0066 in starting with an initial displacement of 0.0066 in. The resulting applied displacement in the final step, 0.066 in, is used to produce a similar total strain as the available computed data.

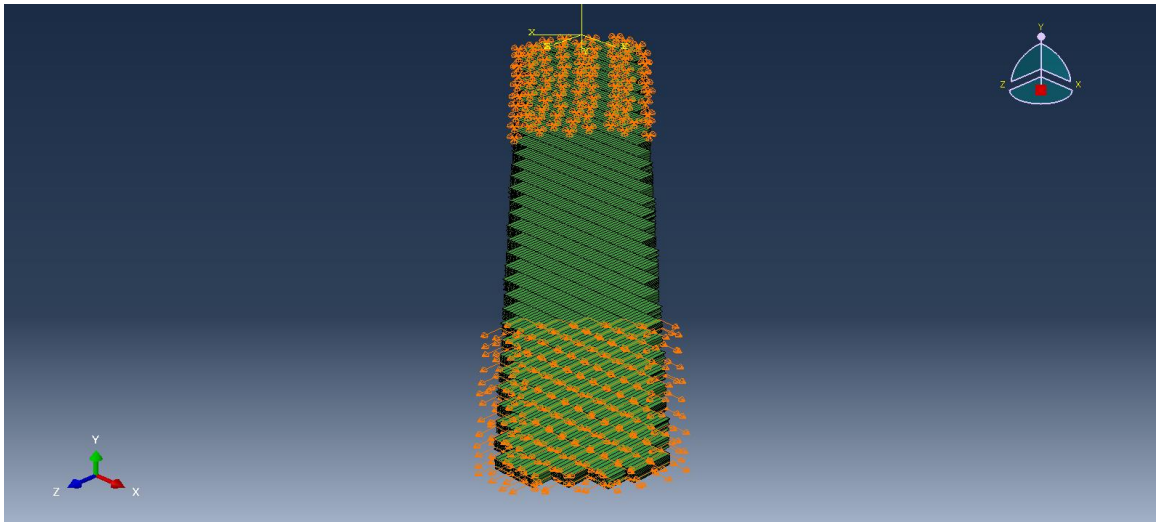

Figure 4.35 Boundary Conditions for Off-Axis Test (45°, 1-2 Plane)

The test details and results for the fine mesh are discussed below.

Table 4.19 Model Parameters

Parameter	Value
a	0.03737 in
r_{fiber}	0.01549 in
L	4.5 in
L_{TAB}	1.25 in
n_{rows}	2
$n_{columns}$	14

Table 4.20 Model Size Information

Category for entire model	Value
Total number of nodes	670,692
Total number of elements	672,976
Number of C3D6 elements in fiber	95,952
Number of C3D8 elements in fiber	384,528
Number of C3D8 elements in matrix	192,496

The elements used in generating the homogenized material properties for the test are shown in red in Figure 4.36.

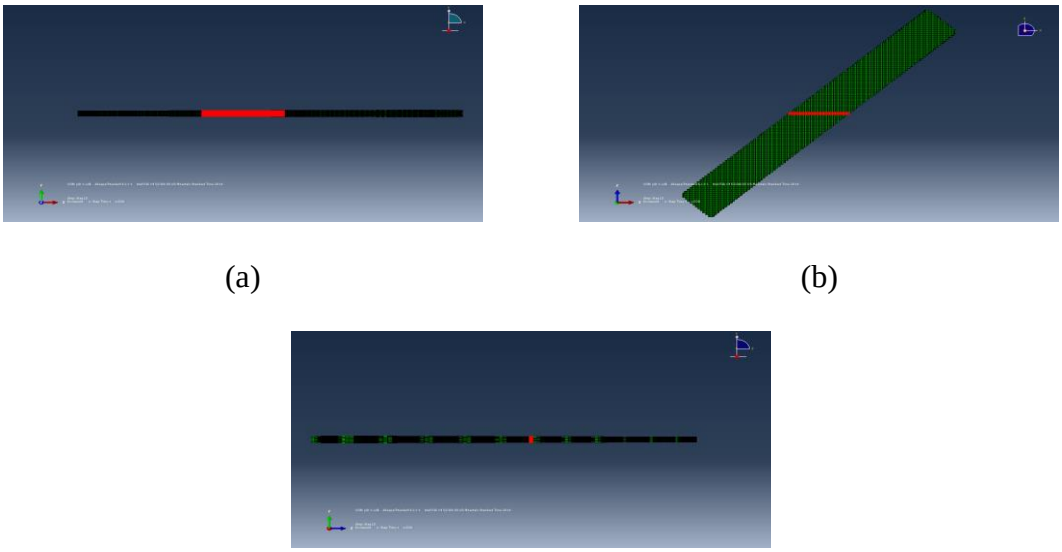

(a) (b)

(c)

Figure 4.36 Section View of (a) x-y (b) x-z and (c) z-y Planes of the Elements used in Computing the Homogenized Material Properties

The homogenized engineering stress-strain curve is plotted along with the available computed data (Goldberg, 2013) in Figure 4.37.

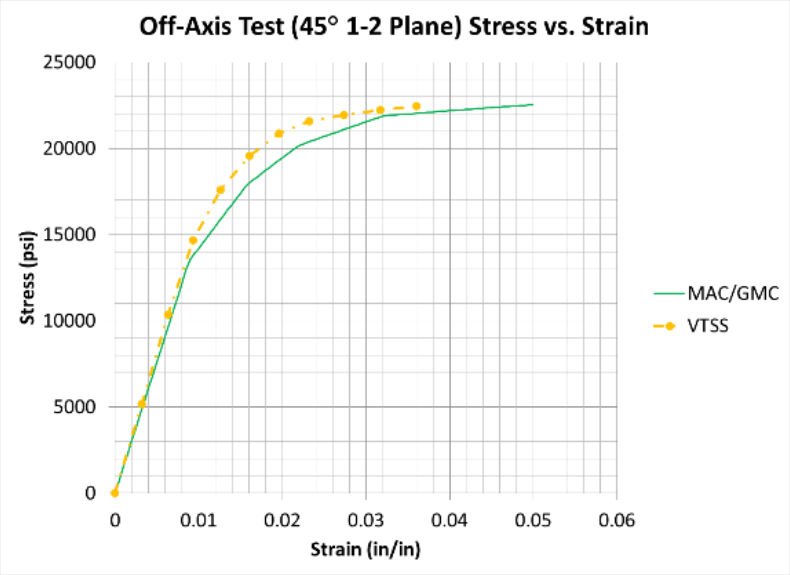

Figure 4.37 Stress vs. Strain $\left(\sigma_{(45°,1-2)} \text{ vs. } \varepsilon_{(45°,1-2)}\right)$

The stress $\left(\sigma_{(45°,1-2)}\right)$ distribution plotted on the deformed shape of the final step of analysis is shown in Figure 4.38.

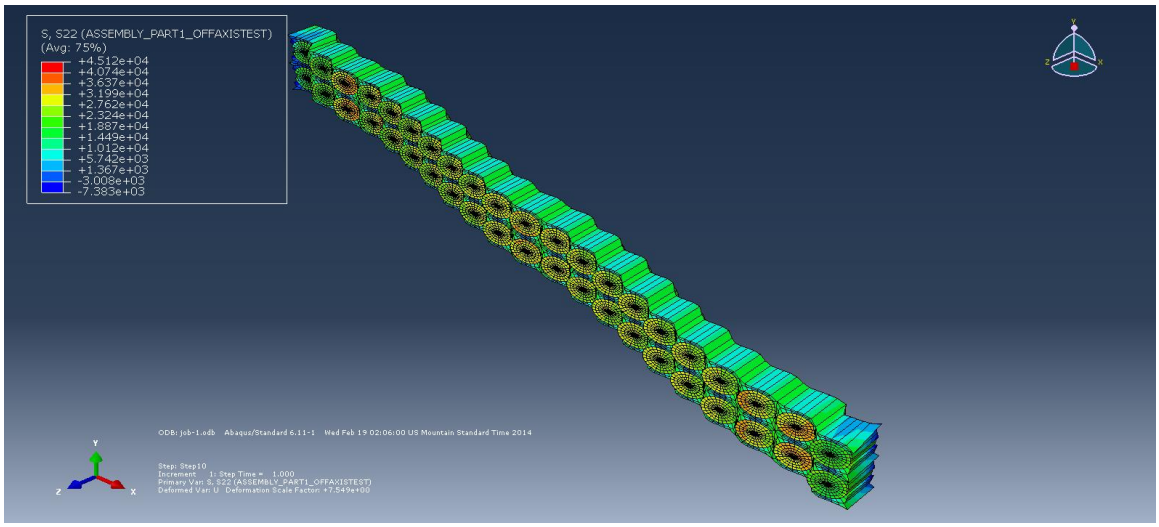

Figure 4.38 Stress $\left(\sigma_{(45°,1-2)}\right)$ Distribution in the Post-Processed Region

The strain $\left(\varepsilon_{(45°,1-2)}\right)$ distribution plotted on the deformed shape of the final step of analysis is shown in Figure 4.39.

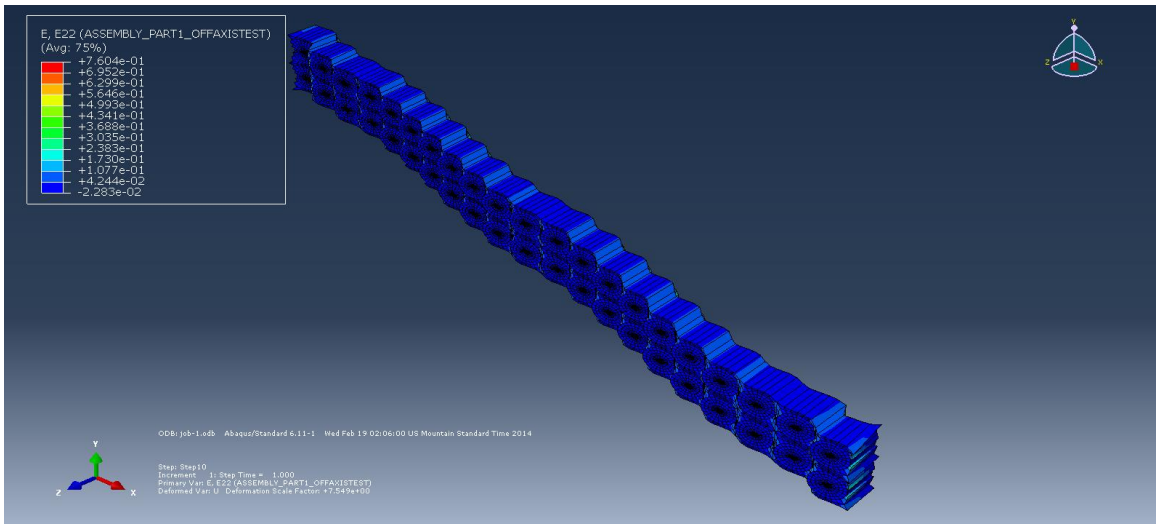

Figure 4.39 Strain $\left(\varepsilon_{(45°,1-2)}\right)$ Distribution in the Post-Processed Region

4.2.4.11 Off-Axis Test – 45°, 2-3 Plane

A displacement controlled analysis is carried out. Displacements are applied to the nodes in the displacement section in the test direction (45°) in ten equal steps of 0.0061 in starting with an initial displacement of 0.0061 in. The resulting applied displacement in the final step, 0.061 in, is used to produce a similar total strain as the available computed data for the tension test in the 2-direction, because the response of this test should be similar due to the transverse isotropy.

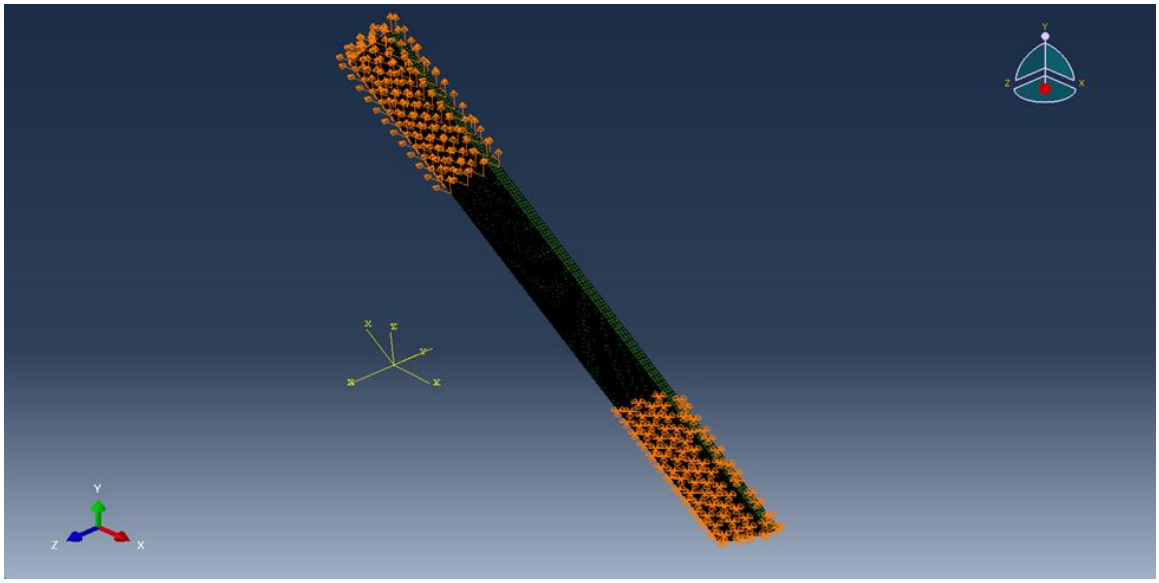

Figure 4.40 Boundary Conditions for Off-Axis Test (45°, 2-3 Plane)

The test details and results for the fine mesh are discussed below.

Table 4.21 Model Parameters

Parameter	Value
a	0.03737 in
r_{fiber}	0.01549 in
L	0.075 in
L_{TAB}	1.25 in
n_{rows}	14
$n_{columns}$	121

Table 4.22 Model Size Information

Category for entire model	Value
Total number of nodes	631,548
Total number of elements	660,960
Number of C3D6 elements in fiber	218,880
Number of C3D8 elements in fiber	220,880
Number of C3D8 elements in matrix	221,200

The elements used in generating the homogenized material properties for the test are shown in red in Figure 4.41.

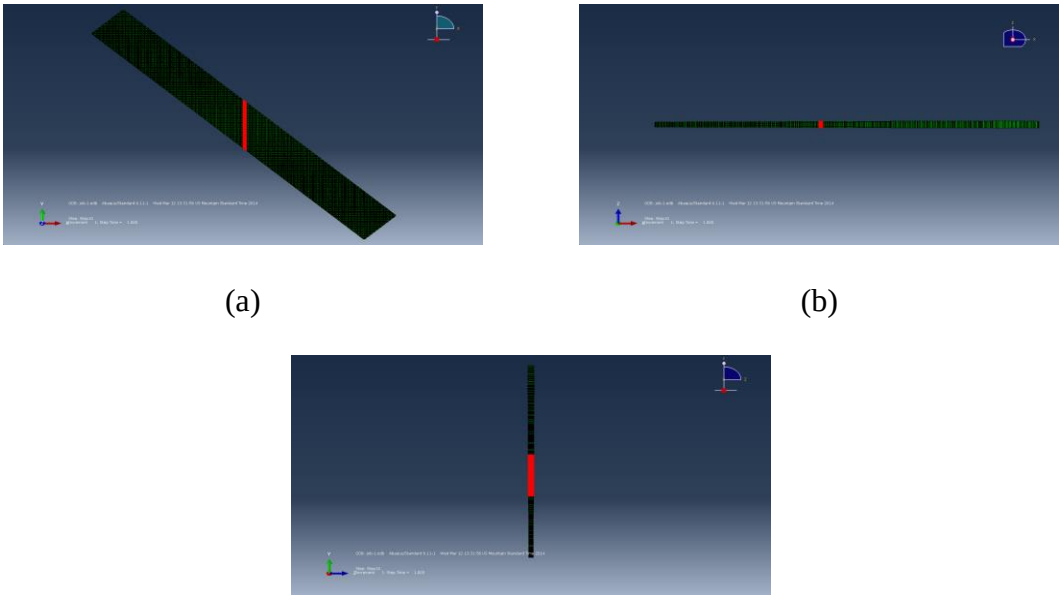

(a) (b)

(c)

Figure 4.41 Section View of (a) x-y (b) x-z and (c) z-y Planes of the Elements used in Computing the Homogenized Material Properties

The homogenized engineering stress-strain curve is plotted in Figure 4.42.

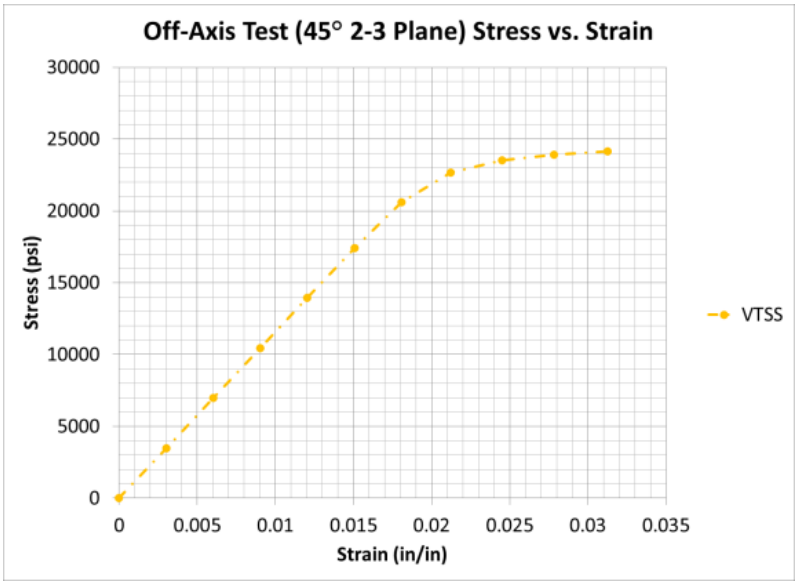

Figure 4.42 Stress vs. Strain $\left(\sigma_{(45°,2-3)} \text{ vs. } \varepsilon_{(45°,2-3)}\right)$

The stress $\left(\sigma_{(45°,2-3)}\right)$ distribution plotted on the deformed shape of the final step of analysis is shown in Figure 4.43.

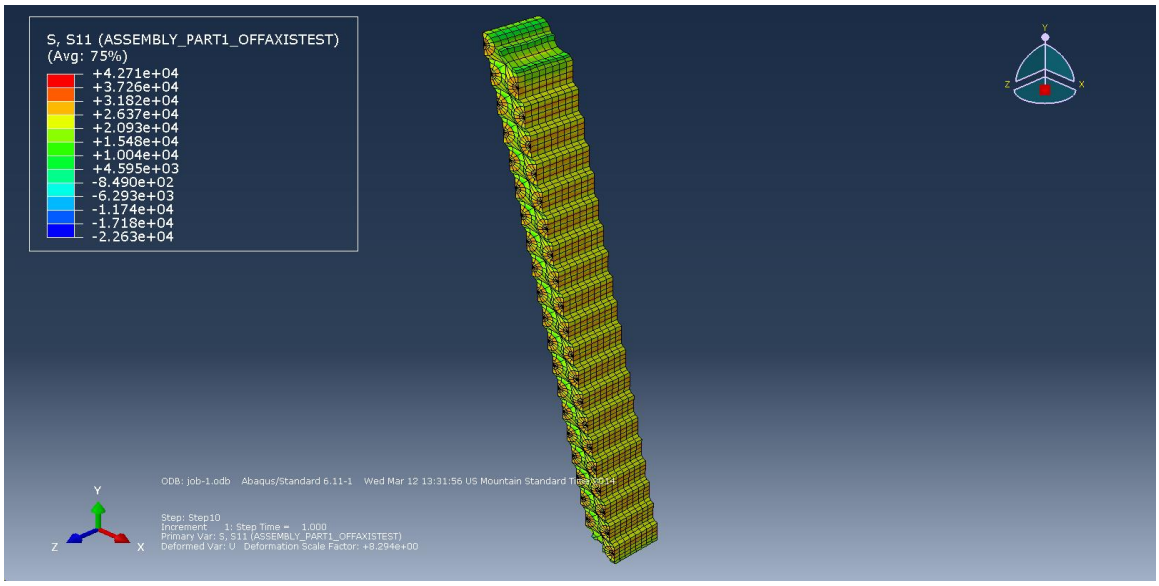

Figure 4.43 Stress $\left(\sigma_{(45°,2-3)}\right)$ Distribution in the Post-Processed Region

The strain $\left(\varepsilon_{(45°,2-3)}\right)$ distribution plotted on the deformed shape of the final step of analysis is shown in Figure 4.44.

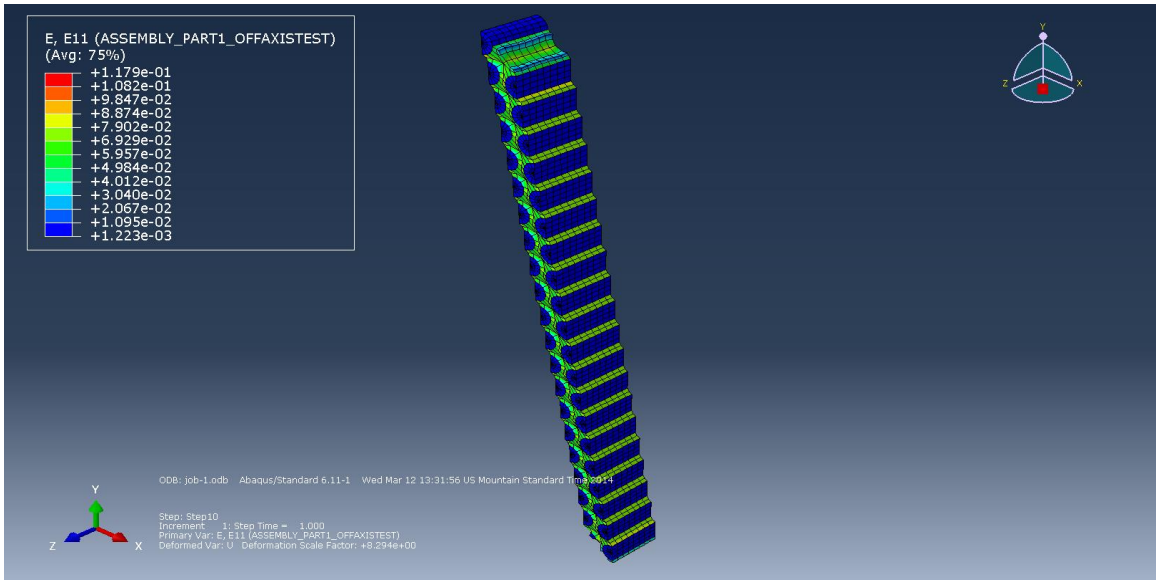

Figure 4.44 Strain $\left(\varepsilon_{(45°,2-3)}\right)$ Distribution in the Post-Processed Region

4.2.4.12 Off-Axis Test – 45°, 1-3 Plane

This test is not necessary because of the transverse isotropy of the composite material (same as the pure shear in the 1-2 plane test).

4.2.5 Polymer Plasticity Model Tests

The aforementioned polymer plasticity model, which accounts for hydrostatic stress effects, is implemented as a user-defined material (umat) in LS-DYNA.

4.2.5.1 Test Details

Plane stress models are analyzed using implicit analysis to test the umat. The schematic of the tension test FE model is shown in Figure 4.45.

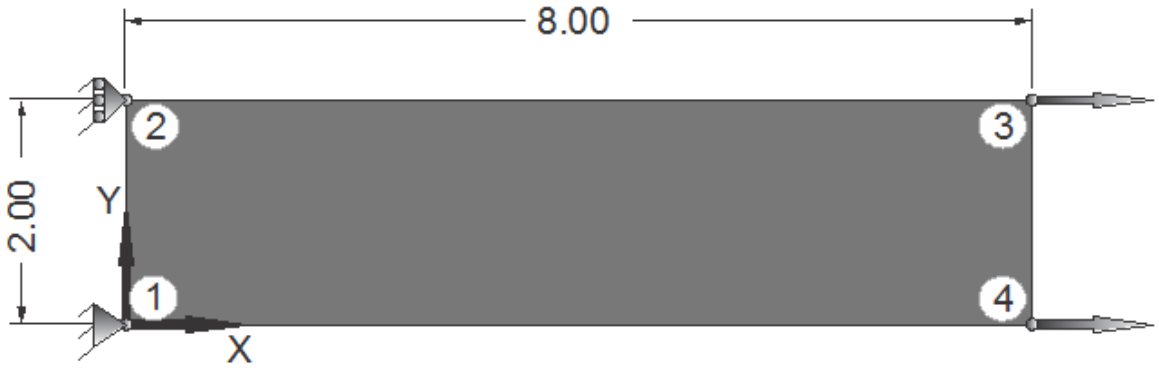

Figure 4.45 Schematic of Tension Test FE Model

Node 1 is pinned. The remaining nodes on the Node 1-2 side are rollers fixed in the x-direction. Displacements are applied to the nodes on the Node 3-4 side in the x-direction.

The schematic of the shear test FE model is shown in Figure 4.45.

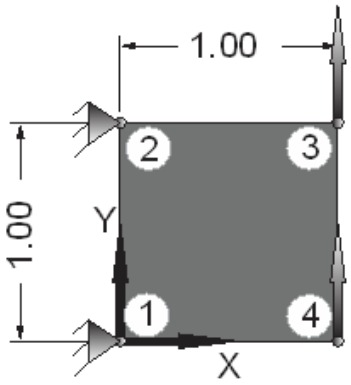

Figure 4.46 Schematic of Shear Test FE Model

Nodes on the Node 1-2 side are pinned. Displacements are applied to the nodes on the Node 3-4 side in the y-direction.

4.2.5.2 Verification Tests

To verify the umat, the PR520 composite material results (R. Goldberg et al., 2005) are replicated using the reported material constants listed in Table 4.23.

Table 4.23 PR520 Matrix Polymer Plasticity Model Material Constants

Modulus (GPA)	Poisson's Ratio	D_0 (1/sec)	n	Z_1 (MPA)	Z_0 (MPA)	q	α_1	α_0
3.54	0.38	$1x10^6$	0.93	753.82	396.09	279.26	0.126	0.568

Shell elements with element formulation (ELFORM) 12 – plane stress (x-y plane) are used. The shell thickness is taken as 0.1 in. The results from the umat along with the experimental and computed results presented in the paper are shown in Figure 4.47.

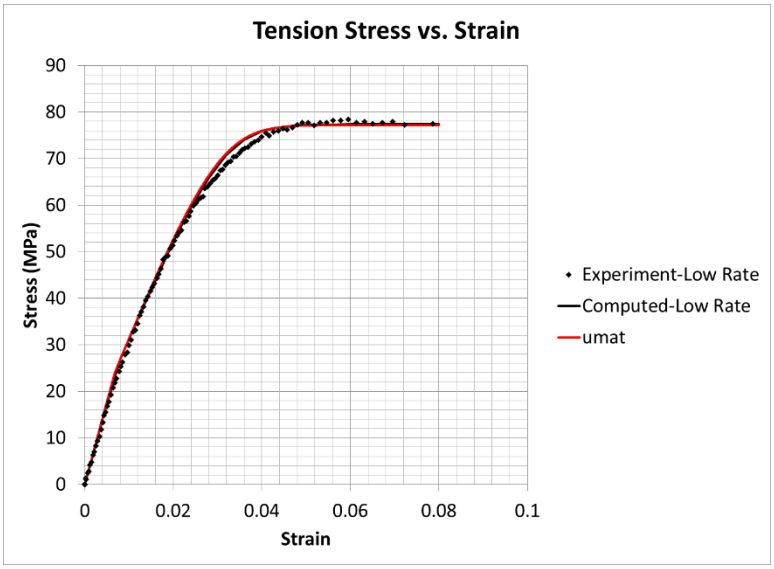

(a)

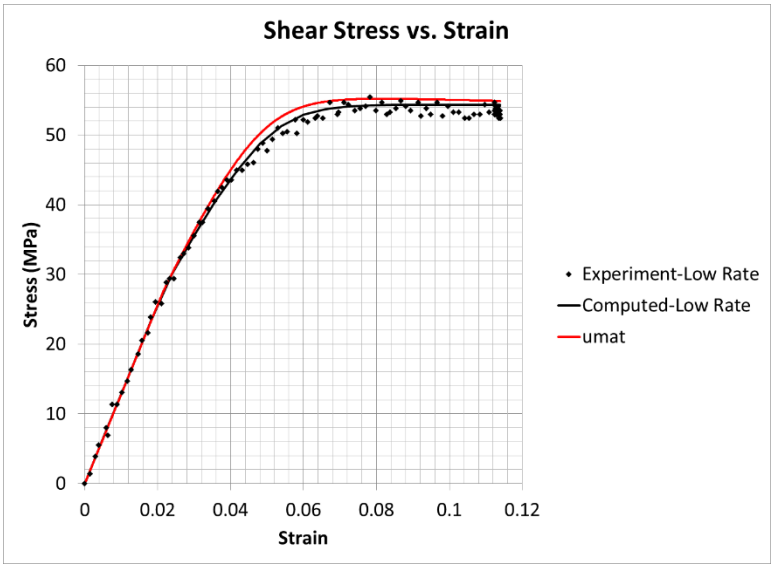

(b)

Figure 4.47 (a) Tension and (b) Shear PR520 Matrix Test Results

4.2.5.3 Validation Tests

To validate the umat, the T800S/3900 matrix is used with material constants calculated using the procedure detailed in the associated report (R. Goldberg et al., 2005). The results are shown in Table 4.24.

Table 4.24 T800S/3900 Matrix Polymer Plasticity Model Material Constants

Modulus (Msi)	Poisson's Ratio	D_0 (1/sec)	n	Z_1 (Msi)	Z_0 (Msi)	q	α_1	α_0
0.5	0.35	$1.8x10^6$	0.33	4.21	4.01	179.8	0.423	0.423

As evidenced in Table 4.3, experimental data is only available for tension in the 1-direction and pure shear in the 1-2 plane tests. For this reason, these tests were selected for comparison between the umat results and the provided experimental and computed data. The tests are completed using the polymer plasticity model for the matrix and the VTSS formulation outlined in the Test Details and Results section. The stress-strain curve for the von Mises (J2) and polymer plasticity models is shown in Figure 4.48.

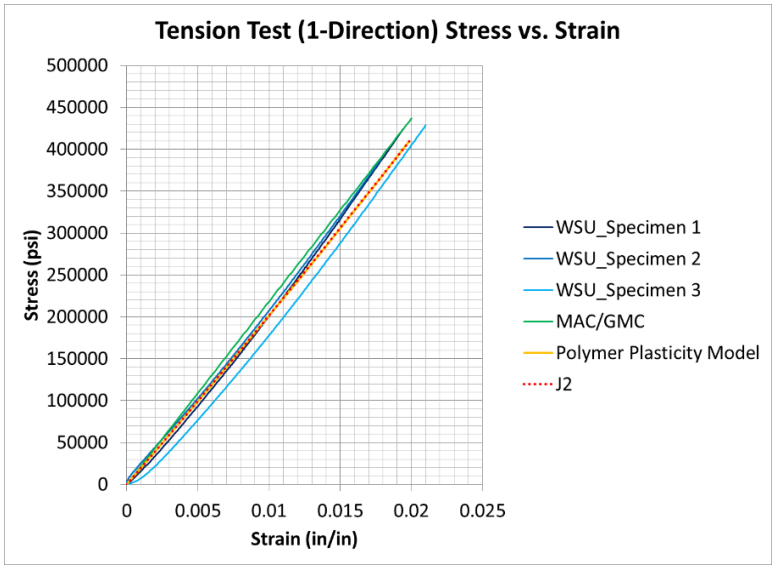

Figure 4.48 Stress vs. Strain Curve for Tension in the 1-Direction Test

5 CONCLUSIONS

The results from the VTSS show good agreement with the elastic constants in the verification test case. It is evident that the difference in fiber placement between the two approaches (random in the virtual framework formulation and uniform in the VTSS) does not significantly impact the results. When comparing the FEM Big and VTSS results, all engineering constants, with the exception of ν_{23}, are within 7% of each other. The difference between the FEM Big and FEM Small results for ν_{23} is also significantly larger compared to the other engineering constants. Furthermore, the value for ν_{23} from the VTSS results is much closer to that of the FEM Small result. From the close proximity of the results, it is clear that the associated extensive constraints implemented by the virtual framework is unnecessary to accurately predict the engineering constants of the composite material.

The VTSS was able to successfully validate the available experimental and computed results for the T800S/3900 composites and fill-in necessary gaps. For example, the off-axis 2-3 plane test is very difficult to complete and there is no experimental data available. The analytical approach makes the assumption that it is the same as the tension in the 2-direction test. As shown by the stress-strain curve generated by the VTSS for the off-axis 2-3 plane test, the yield stress is actually lower than in the tension in the 2-direction test. In this way, further accuracy in the stress-strain input curves is provided by the VTSS.

The polymer plasticity model was successfully validated using a plane stress model for the PR520 matrix. The slight difference in results for the shear test can likely

be attributed to the difficulty of producing a pure shear stress state in a finite element test. This was not an issue for the standalone program used to generate the computed results presented in the report because the formulation allows for directly prescribing the stress state. Using the polymer plasticity model for the T800S/3900 matrix showed good agreement between the stress-strain curves for the von Mises (J2) and polymer plasticity models for the tension test case. However, the pure shear test case failed to converge, indicating that the calculation of the material constants was not representative of the composite material. Physical testing of the constituents is required to use the polymer plasticity model for the T800S/3900 composite. Convergence in the tension case is expected because the only change from the von Mises plasticity models is in the matrix material model, and the fibers carry the majority of the stress in the 1-direction tension test.

5.1 Future Work

The VTSS is currently limited to unidirectional laminated composite architectures. The immediate focus for future work of this research topic would be extending the geometry capabilities. Developing support for angle-ply composite architectures would allow for further validation tests using the available experimental data from WSU.

Another limitation of this method is the absence of damage. The focus of many available virtual testing suites is this component, which can be added to increase the accuracy of the model.

REFERENCES

Aboudi, J. (2004). The Generalized Method of Cells and High-Fidelity Generalized Method of Cells Micromechanical Models--A Review. *Mechanics of Advanced Materials & Structures*, *11*(4/5), 329–366.

Adams, D. (2009). *Direct measurement of laminate through-thickness tensile strength*. Retrieved from http://www.compositesworld.com/articles/direct-measurement-of-laminate-through-thickness-tensile-strength

Bednarcyk, B. A., NASA Glenn Research Center, & United States. (2012). *A multiscale, nonlinear, modeling framework enabling the design and analysis of composite materials and structures*. Cleveland, Ohio: National Aeronautics and Space Administration, Glenn Research Center.

Coenen, E. W. C., Kouznetsova, V. G., & Geers, M. G. D. (2012). Multi-scale continuous–discontinuous framework for computational-homogenization–localization. *Journal of the Mechanics and Physics of Solids*, *60*(8), 1486–1507. doi:10.1016/j.jmps.2012.04.002

D30 Committee. (2007). *Test Method for Through-Thickness Flatwise Tensile Strength and Elastic Modulus of a Fiber-Reinforced Polymer Matrix Composite Material*. ASTM International. Retrieved from http://www.astm.org/Standards/D7291.htm

D30 Committee. (2008). *Test Method for Compressive Properties of Polymer Matrix Composite Materials with Unsupported Gage Section by Shear Loading*. ASTM International. Retrieved from http://www.astm.org/Standards/D3410.htm

D30 Committee. (2011). *Test Method for Flatwise Compressive Properties of Sandwich Cores*. ASTM International. Retrieved from http://www.astm.org/Standards/C365.htm

D30 Committee. (2013). *Test Method for Shear Properties of Composite Materials by the V-Notched Beam Method*. ASTM International. Retrieved from http://www.astm.org/Standards/D5379.htm

D30 Committee. (2014). *Test Method for Tensile Properties of Polymer Matrix Composite Materials*. ASTM International. Retrieved from http://www.astm.org/Standards/D3039.htm

Davies, G. a. O., & Ankersen, J. (2008). Virtual testing of realistic aerospace composite structures. *Journal of Materials Science*, *43*(20), 6586–6592. doi:10.1007/s10853-008-2695-x

Duschlbauer, D., BÖhm, H. J., & Pettermann, H. E. (2006). Computational Simulation of Composites Reinforced by Planar Random Fibers: Homogenization and Localization by Unit Cell and Mean Field Approaches. *Journal of Composite Materials*, *40*(24), 2217–2234. doi:10.1177/0021998306062317

Eshelby, J. D. (1957). The Determination of the Elastic Field of an Ellipsoidal Inclusion, and Related Problems. *Proceedings of the Royal Society of London. Series A, Mathematical and Physical Sciences*, *241*(1226), 376–396.

Goldberg, R. K. (2013). T800S/3900 Characterization Procedures and Results. National Aeronautics and Space Administration, Glenn Research Center.

Goldberg, R. K., Carney, K. S., Du Bois, P., Hoffarth, C., Harrington, J., Rajan, S. D., & Blankenhorn, G. (2014). Theoretical Development of an Orthotropic Elasto-Plastic Generalized Composite Material Model. Presented at the 13th International LS-DYNA Users Conference, Dearborn, MI.

Goldberg, R., Roberts, G., & Gilat, A. (2005). Implementation of an Associative Flow Rule Including Hydrostatic Stress Effects into the High Strain Rate Deformation Analysis of Polymer Matrix Composites. *Journal of Aerospace Engineering*, *18*(1), 18–27. doi:10.1061/(ASCE)0893-1321(2005)18:1(18)

Hill, R. (1963). Elastic properties of reinforced solids: Some theoretical principles. *Journal of the Mechanics and Physics of Solids*, *11*(5), 357–372. doi:10.1016/0022-5096(63)90036-X

Hoffarth, C., Harrington, J., Rajan, S. D., Goldberg, R. K., Carney, K. S., Du Bois, P., & Blankenhorn, G. (2014). Verification and Validation of a Three-Dimensional Generalized Composite Material Model. Presented at the 13th International LS-DYNA Users Conference, Dearborn, MI.

Karkkainen, R. L., Moy, P., & Tzeng, J. T. (2009). *Through-Thickness Property Measurement of Three-Dimensional Textile Composites* (Final No. ARL-TR-4765). Army Research Laboratory.

Llorca, J., González, C., Molina-Aldareguía, J. M., & Lópes, C. S. (2013). Multiscale Modeling of Composites: Toward Virtual Testing ... and Beyond. *JOM*, *65*(2), 215–225.

LLorca, J., González, C., Molina-Aldareguía, J. M., Segurado, J., Seltzer, R., Sket, F., … Canal, L. P. (2011). Multiscale Modeling of Composite Materials: a Roadmap Towards Virtual Testing. *Advanced Materials*, *23*(44), 5130–5147. doi:10.1002/adma.201101683

Melro, A. R., Camanho, P. P., & Pinho, S. T. (2012). Influence of geometrical parameters on the elastic response of unidirectional composite materials. *Composite Structures*, *94*(11), 3223–3231. doi:http://dx.doi.org.ezproxy1.lib.asu.edu/10.1605/01.301-0019924118.2012

Neto, E. de S., Periæ, P. D., & Owen, P. D. (2009). *Computational Methods for Plasticity: Theory and Applications*. John Wiley & Sons.

Okereke, M. I., & Akpoyomare, A. I. (2013). A virtual framework for prediction of full-field elastic response of unidirectional composites. *Computational Materials Science*, *70*, 82–99. doi:10.1016/j.commatsci.2012.12.036

Raju, K. S., & Acosta, J. F. (2010). *Crashworthiness of Composite Fuselage Structures—Material Dynamic Properties, Phase I*. Presented at the National Technical Information Service, Washington.

Suquet, P. M. (1985). Local and global aspects in the mathematical theory of plasticity. *Plasticity Today: Modelling, Methods and Applications*, 279–310.

Torayca. (2003). T800S Data Sheet (Technical Data Sheet No. CFA-019).

Vali-shariatpanahi, S. (2009). Determination of through thickness properties for composite thick laminate. In *Industry*. Edinburgh, Scotland.

Voigt, W. (1890). Ueber die Beziehung zwischen den beiden Elasticitätsconstanten isotroper Körper. *Journal de Physique Théorique et Appliquée*, *9*(1), 201–202. doi:10.1051/jphystap:018900090020100

Yang, Q. D., Cox, B. N., Fang, X. J., & Zhou, Z. Q. (2010). Virtual Testing for Advanced Aerospace Composites: Advances and Future Needs. *Journal of Engineering Materials and Technology*, *133*(1), 011002–011002. doi:10.1115/1.4002637

APPENDIX A

REQUIRED TEST AND RESULTING INPUT FOR MAT213

Test	Resulting Input for MAT213
Tension (1-direction)	Tension stress-strain curve $\left(\sigma_{11}^{T} \text{ vs. } \varepsilon_{11}^{T}\right)$
	Yield strain $\left(\varepsilon_{11}\right)_{y}^{T}$ and optionally yield stress $\left(\sigma_{11}\right)_{y}^{T}$
	Elastic Poisson's ratio $\left(\nu_{12}, \nu_{13}\right)$
	Plastic Poisson's ratio $\left(\nu_{12}^{p}, \nu_{13}^{p}\right)$
Tension (2-direction)	Tension stress-strain curve $\left(\sigma_{22}^{T} \text{ vs. } \varepsilon_{22}^{T}\right)$
	Yield strain $\left(\varepsilon_{22}\right)_{y}^{T}$ and optionally yield stress $\left(\sigma_{22}\right)_{y}^{T}$
	Elastic Poisson's ratio $\left(\nu_{23}\right)$
	Plastic Poisson's ratio $\left(\nu_{21}^{p}, \nu_{23}^{p}\right)$
Tension (3-direction)	Tension stress-strain curve $\left(\sigma_{33}^{T} \text{ vs. } \varepsilon_{33}^{T}\right)$
	Yield strain $\left(\varepsilon_{33}\right)_{y}^{T}$ and optionally yield stress $\left(\sigma_{33}\right)_{y}^{T}$
	Plastic Poisson's ratio $\left(\nu_{32}^{p}, \nu_{31}^{p}\right)$

Compression (1-direction)	Compression stress-strain curve $\left(\sigma_{11}^{C} \text{ vs. } \varepsilon_{11}^{C}\right)$
	Yield strain $\left(\varepsilon_{11}\right)_{y}^{C}$ and optionally yield stress $\left(\sigma_{11}\right)_{y}^{C}$
Compression (2-direction)	Compression stress-strain curve $\left(\sigma_{22}^{C} \text{ vs. } \varepsilon_{22}^{C}\right)$
	Yield strain $\left(\varepsilon_{22}\right)_{y}^{C}$ and optionally yield stress $\left(\sigma_{22}\right)_{y}^{C}$
Compression (3-direction)	Compression stress-strain curve $\left(\sigma_{33}^{C} \text{ vs. } \varepsilon_{33}^{C}\right)$
	Yield strain $\left(\varepsilon_{33}\right)_{y}^{C}$ and optionally yield stress $\left(\sigma_{33}\right)_{y}^{C}$
Shear(1-2 plane)	Shear stress-strain curve $\left(\sigma_{12} \text{ vs. } \varepsilon_{12}\right)$
	Yield strain $\left(\varepsilon_{12}\right)_{y}$ and optionally yield stress $\left(\sigma_{12}\right)_{y}$
Shear (2-3 plane)	Shear stress-strain curve $\left(\sigma_{23} \text{ vs. } \varepsilon_{23}\right)$
	Yield strain $\left(\varepsilon_{23}\right)_{y}$ and optionally yield stress $\left(\sigma_{23}\right)_{y}$

Shear (1-3 plane)	Shear stress-strain curve $\left(\sigma_{31} \text{ vs. } \varepsilon_{31}\right)$
	Yield strain $\left(\varepsilon_{31}\right)_y$ and optionally yield stress $\left(\sigma_{31}\right)_y$
Off-axis tension (45°, 1-2 plane)	Off-axis tension stress-strain curve $\left(\sigma_{45}^{1-2} \text{ vs. } \varepsilon_{45}^{1-2}\right)$
	Yield strain $\left(\varepsilon_{45}^{1-2}\right)_y$ and optionally yield stress $\left(\sigma_{45}^{1-2}\right)_y$
Off-axis tension (45°, 2-3 plane)	Off-axis tension stress-strain curve $\left(\sigma_{45}^{2-3} \text{ vs. } \varepsilon_{45}^{2-3}\right)$
	Yield strain $\left(\varepsilon_{45}^{2-3}\right)_y$ and optionally yield stress $\left(\sigma_{45}^{2-3}\right)_y$
Off-axis tension (45°, 1-3 plane)	Off-axis tension stress-strain curve $\left(\sigma_{45}^{1-3} \text{ vs. } \varepsilon_{45}^{1-3}\right)$
	Yield strain $\left(\varepsilon_{45}^{2-3}\right)_y$ and optionally yield stress $\left(\sigma_{45}^{2-3}\right)_y$

APPENDIX B

CONVERGENCE STUDY STRESS-STRAIN CURVES

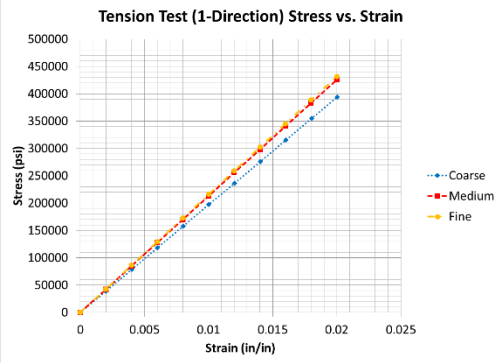

(1a)

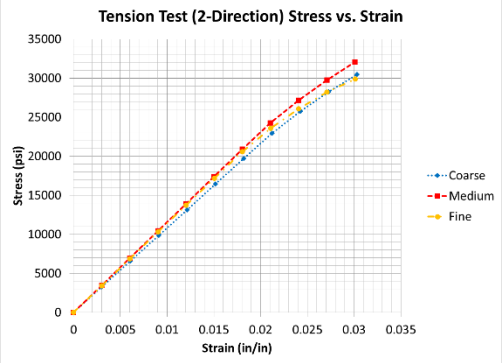

(1b)

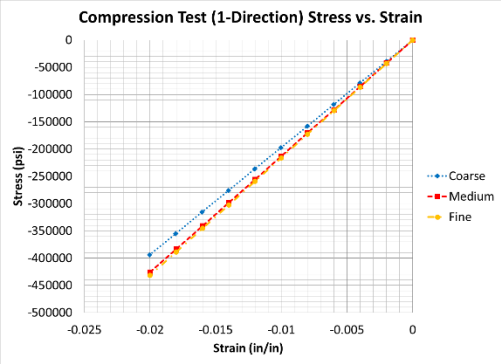

(2a)

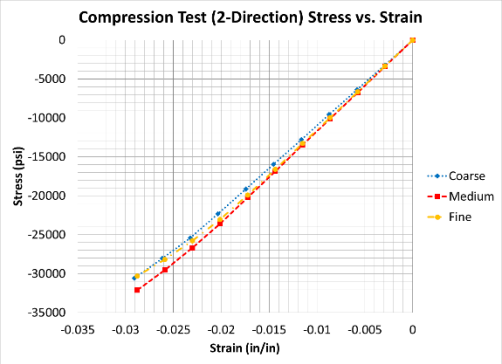

(2b)

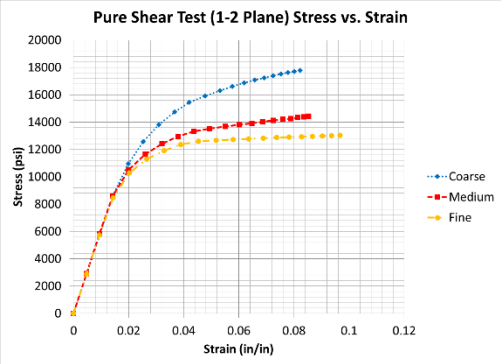

(3a)

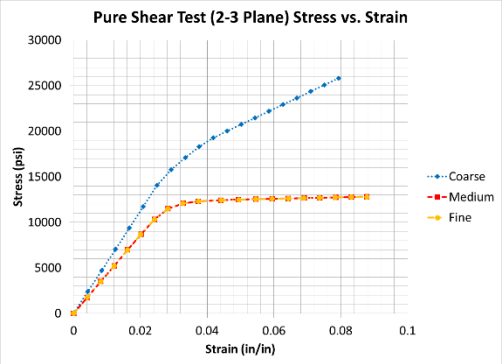

(3b)

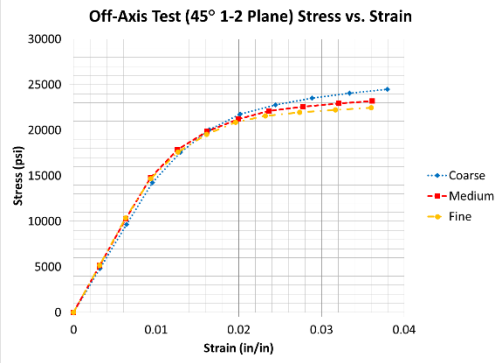

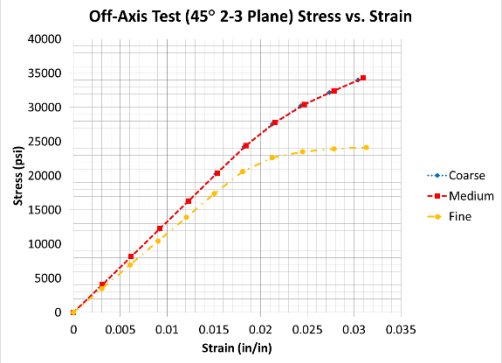

(4a) (4b)

(1) Tension Tests in the (a) 1 and (b) 2-directions, (2) Compression Tests in the (a) 1 and (b) 2-Directions, (3) Pure Shear Tests in the (a) 1-2 and (b) 2-3 Planes, and (4) Off-Axis Tests in the (a) 1-2 and 2-3 Planes